RSC Advances

PAPER

View Article Online
View Journal | View Issue

Check for updates

Cite this: *RSC Adv.*, 2026, **16**, 14328

Catechol functionalized polyguluronate enriched sodium alginate wetspun fibers with immobilized platelet lysate for diabetic wound healing

Hafsa Khanam,[a] Ashraful Hoque,[b] Mohammad A. Jafar Mazumder[cd] and M. Tarik Arafat *[a]

Received 30th January 2026
Accepted 9th March 2026

DOI: 10.1039/d6ra00827e

rsc.li/rsc-advances

The development of advanced wound dressings with multifunctional properties is crucial for accelerating healing in diabetic wounds. Platelet lysate contains many biologically active substances, which have tremendous clinical benefits in treating diabetic wounds. However, its clinical use and therapeutic efficacy are severely limited by its poor mechanical qualities and the sudden release of active chemicals. To address these challenges and minimize the risk of wound infection, sodium alginate–polyethylene glycol wetspun fibers were developed and immobilized with platelet lysate. Furthermore, surface modification with dopamine introduced catechol groups, enhancing interfacial adhesion and bioactivity to promote effective healing in diabetic wounds. Morphological and physicochemical analyses confirmed improved thermal stability and crystalline behavior in the dopamine modified fibers (SA-PEG-D-PL). The modified fibers achieved sustained PL release over 18 days with 90% cumulative release, a 30% improvement over free PL and a 20% improvement over unmodified fibers. The whole blood clotting index demonstrated a notably lower BCI of 15% for dopamine functionalized fibers, indicating enhanced coagulation potential due to increased surface striation and water absorption. Moreover, in a diabetic mice wound model, the functionalized fibers drove >85% wound closure by day 7 and complete reepithelialization by day 14, while reducing scar formation to a scar index of 7.3, significantly lower than controls (22–42.6). These outcomes suggest that the synergistic effects of dopamine functionalization and PL immobilization on alginate based fibrous matrices not only improve mechanical and biological responses but also accelerate wound closure and minimize scarring. Overall, the developed dopamine modified fibers demonstrate high potential as an advanced wound care material for diabetic patients.

1. Introduction

Diabetic wounds affect millions of people worldwide, creating a substantial and growing socioeconomic burden. Recurrent ulcer infections can lead to serious consequences, including amputation and a higher risk of death.[1] These wounds are further complicated by a multifactorial pathological environment, including lack of growth factors (GFs), decreased microvasculature, increased pro-inflammatory cytokines and proteases, compromised cellular functioning, and microbial invasion.[2,3] Consequently, there is a delay in the shift from the inflammatory to the proliferative phase of wound healing.[4] As primary inflammatory cells, macrophages are essential for triggering inflammatory responses during wound healing processes.[5] Their morphologies vary, with M1 macrophages encouraging inflammation and M2 macrophages aiding in wound healing.[6] The control of macrophage polarization from M1 to M2 phenotypes is therefore critical for the healing of diabetic wounds.

Platelet lysate is a complex mixture of proteins and growth factors derived from lysed platelets. As corpuscular blood components, platelets are crucial for wound healing, tissue regeneration, and the control of hemostasis and clot formation during bleeding.[7] PL's high amounts of growth factors, which interact with tyrosine-kinase receptors to promote cell proliferation and inhibit apoptosis, are the reason for its widespread use as a serum substitute. Mechanistically, GFs bind to cell protein tyrosine kinase receptors and trigger intracellular events, making them very attractive molecules for use in manipulating cell behavior.[8] Platelet-derived growth factors (PDGFs) recruit neutrophils and macrophages to the wound *via*

---

[a] *Department of Biomedical Engineering, Bangladesh University of Engineering and Technology (BUET), Dhaka-1205, Bangladesh. E-mail: tarikarafat@bme.buet.ac.bd; Tel: +880255167100 Ext.6133*

[b] *National Institute of Burn and Plastic Surgery, Dhaka 1205, Bangladesh*

[c] *Department of Chemistry, King Fahd University of Petroleum & Minerals (KFUPM), Dhahran 31261, Saudi Arabia*

[d] *Interdisciplinary Research Center for Refining and Advanced Chemicals, King Fahd University of Petroleum & Minerals (KFUPM), Dhahran 31261, Saudi Arabia*

chemotaxis. VEGFs promote angiogenesis and neurogenesis, while TGF-β1 regulates inflammation, epithelialization, and connective tissue regeneration. EGFs accelerate keratinocyte migration, and cytokines attract immune cells to clear debris.[9,10] However, the short half-life of 95% of these GFs, which are produced within an hour and rapidly dilute and degrade into the tissue fluid, and the burst release of PL limit their applications.[11,12] Platelet rich plasma (PRP) and PL have been incorporated into diverse biomaterial carriers such as injectable hydrogels,[13] electrospun nanofibers,[14] and collagen or chitosan scaffolds,[15] nanoparticles[7] to enhance growth factor delivery for wound repair.

Notably, several recent investigations have attempted to address the fast release of growth factors (GFs) from PRP gels by including extra gel matrices to produce network topologies that penetrate deeply.[16–18] Researchers have also anchored PRP onto scaffold surfaces, including films and foams. However, in comparison to clinical PRP gels, the efficacy was restricted by the weak interfacial interaction between platelets and the scaffold, which only prolonged GF release by roughly three days.[19] Consequently, fiber-based dressings, with their advantageous physicochemical, mechanical, and biological properties, show great promise for the treatment of skin wounds. Wet spinning is one of the various fiber production techniques that may turn biomolecules into fibers without requiring high voltage during production, and is less likely to result in denaturation.[20] Furthermore, it offers greater control over yarn preparation, doping or surface modification, fiber morphology and structure, and other factors, expanding the range of possible applications.[21,22]

Building on the capability of wet spinning to produce continuous, cell interactive fibers, sodium alginate (SA) was selected as the primary. SA is a family of naturally occurring polysaccharides that are taken from seaweed or brown algae. SA chains are made up of copolymers of β-D-mannuronate (M) and its C-5 epimer, a-L guluronate (G), which have a GAG proxy structure.[23] For instance, guluronate (G) blocks of alginate and calcium electrolyte (Ca^{2+}) can combine to produce an egg-box like structure, where the majority of M blocks are left unused.[24] SA releases encapsulated medications and compounds when it comes into contact with a moist environment. It restricts wound secretions and lowers bacterial contamination because of its excellent water absorption capabilities.[25] Polyethylene glycol (PEG) was used as a secondary polymer to provide flexibility and regulated hydration. It has FDA approval for intravenous, oral, and cutaneous use in humans and is harmless.[26] PEG and its derivatives are extensively used in tissue engineering because of their high biocompatibility, which allows them to break down and create a scaffold for the migration of cells during wound healing. It has been documented that PEG based wound healing speeds up wound closure by encouraging skin cells to expand and multiply with collagen deposition, particularly in diabetic wounds.[27]

Scientists have investigated the special qualities of dopamine for possible wound healing applications, motivated by mussels' capacity to stick to a range of surfaces in watery conditions.[28] It has strong self-polymerization properties, and its functionalization and modification procedure have drawn a lot of interest.[29,30] In recent research, DA has been utilized to improve the interfacial interaction between fibers and the composite matrix.[31–33] Due to possible conformational changes or steric obstruction, covalent binding may allow for the more controlled release of GFs. This could have an impact on the GFs' biological activity and how well they interact with cell receptors.[34,35]

Previous studies have demonstrated the potential of silk fibroin and synthetic polymer based fibers for PL delivery; however, their reliance on organic solvents, limited swelling behavior, and poor suitability for chronic diabetic wounds pose significant limitations.[36,37] Nevertheless, there are drawbacks to administering PL straight to the wound site, though. Many wounds have irregular geometry, which makes it difficult to get complete and consistent coverage and may lead to inconsistent therapeutic outcomes. Furthermore, because PL is liquid, keeping it stable at the wound site is difficult because body movements can easily move it. Additionally, works incorporating PRP into PLGA or chitosan-based scaffolds have suffered from burst release and inadequate long term evaluation under physiological conditions.[38,39] To address these gaps, the present study offers an eco friendly and mechanically stable platform with sustained GF release tailored for diabetic wound healing. Even so, surface functionalized wetspun fibers incorporated with PL have not been studied yet. This unexplored combination holds significant potential to enhance GF retention and sustained bioactivity, which are key requirements for effective diabetic wound healing. With the help of moisture, structural support, and an ongoing supply of growth factors, this composite dressing addresses the underlying reasons and the ability to prevent the wastage of GFs.

This study aims to develop SA–PEG fibers *via* wet spinning, with glycerol incorporated to enhance flexibility. PEG was added to improve mechanical compliance, and the polymer solution was extruded into a calcium ion (Ca^{2+}) coagulation bath to achieve ionic cross linking. The fibers were then functionalized with catechol groups using polydopamine (PDA) and immobilized with platelet lysate (PL) to impart bioactivity. Characterizations were conducted to evaluate the morphology, physical, and mechanical properties. Additional assessments, such as *in vitro* PL release and *in vivo* wound healing ability of the fibers in diabetic wounds were investigated.

2. Materials and methods

2.1 Materials

Sodium alginate (SA), dopamine hydrochloride (DA), streptozotocin (STZ), and glycerol were purchased from Sigma-Aldrich. Polyethylene glycol (6000) (PEG), potassium chloride (KCl), sodium chloride (NaCl), disodium hydrogen phosphate (Na_2HPO_4), potassium dihydrogen phosphate (KH_2PO_4), sodium hydroxide pellets (NaOH) were purchased from Merck, Germany. Calcium chloride ($CaCl_2$) was purchased from Loba. Hydrochloric acid (HCl) was purchased from ACI Labscan.

2.2 Preparation of platelet lysate (PL)

Human blood was drawn in compliance with the Declaration of Helsinki and relevant national laws in order to extract PL. With permission number NIBPS-February24/03, the National Institute of Burn & Plastic Surgery's ethical committee gave its consent to the experiments. The study's human subjects gave their informed consent. Platelets were pooled from multiple donors to ensure biological reproducibility and minimize batch-to-batch variability. The initial platelet count in PRP was 2.5×10^9 platelets per mL as determined by an automated hematology analyzer. To prepare PL, the PRP was subjected to three repeated freeze–thaw cycles consisting of freezing at −80 °C followed by thawing at 37 °C to rupture platelet membranes and release bioactive contents (Fig. S1). The lysed suspension was then centrifuged at $3000 \times g$ for 15 minutes at 4 °C to remove platelet debris. The resulting supernatant, rich in growth factors, cytokines, serotonin, adenosine, and histamine, was collected as platelet lysate. To ensure sterility, the PL was filtered through a 0.22 μm sterile filter, aliquoted, and stored at −80 °C until further use.[40,41]

2.3 Fabrication of wetspun fibers

20% PEG and 5% SA solutions were prepared separately in deionized (DI) water. A combined solution was then prepared at SA : PEG ratio of 5 : 3, followed by the addition of 15% glycerol. The mixture was ultrasonicated for 15 minutes to eliminate air bubbles. A 15-gauge stainless steel needle was used to fill a 10 milliliter syringe with the combined solution. Following its extrusion from the nozzle tip, the polymer solution was placed in a coagulation bath that contained 5% $CaCl_2$ solution.[42] Ionic crosslinking occurred primarily through the polyguluronate (G-block) regions of SA. These regions facilitated the formation of stable ‘egg-box’ structures with divalent cations. A gel resembling fibers developed immediately; however, it took some maturation time of three to five minutes. After a careful bath extraction, the wetspun fibers were then rinsed in DI for an additional three to five minutes and dried individually at room temperature for two days. It was named SA–PEG fibers.

2.4 Fabric manufacturing process

Wetspun fibers were gathered and allowed to dry before being used to make fabric. SA–PEG fibers were woven into two-dimensional textile structures using a manual handloom setup, with controlled tension to guarantee consistency. Tight interlacing and constant spacing were maintained by carefully adjusting the warp and weft alignment. Exact control over the overall fabric architecture and weave density was made possible by the handloom process. The purpose of this fabric construction was to improve mechanical integrity and offer an appropriate platform for long term release of biomolecules and cell contact in wound healing applications.

2.5 Catechol functionalization and PL immobilization

SA–PEG fabrics were collected and immersed in 0.01 M NaOH for half an hour. NaOH treatment resulted in an increase in hydroxyl and carboxyl functional groups on the polymer chain, which in turn boosted DA adherence.[43] A solution containing 2 mg mL^{-1} of dopamine hydrochloride was produced in an aqueous medium. Basic circumstances allow DA to self-polymerize.[44] Consequently, 10 mM of Tris–HCl was added to the solution to bring its pH down to 8.5. After being partially submerged in the DA solution, the functionalized SA–PEG fabrics were left in an incubator set to 37 °C for three hours. After that, DI water was used to rinse these fabrics three times. Then, the surface modified (SA-PEG-D) fabrics were immersed in activated PL, ensuring that those fibers were fully immersed. Kept it in the incubator for two hours and dried at room temperature, and the fabric was named SA-PEG-D-PL.

3. Characterization

3.1 Field emission scanning electron microscopy (FESEM)

The surface morphology of the fibers was examined using FESEM (Zeiss Sigma 300 VP) with an acceleration voltage of 2 kV. To improve conductivity and lessen charging effects, a small layer of gold was sputter-coated onto the samples before imaging. The fibers were examined at different magnifications. The images were examined for surface striation, and any structural alterations following PL inclusion or surface modification with DA. Observing how the crosslinking and modification operations affected the surface integrity and uniformity of the fibers received particular focus. Fiber diameters were measured from the FESEM images using ImageJ software. The average of the standard deviation (SD) was used to depict the data.

3.2 Attenuated total reflection Fourier transformation infrared spectroscopy analysis (ATR-FTIR)

The chemical composition of the DA modified and unmodified fibers was analyzed by ATR-FTIR using Nicolet iS5 FTIR Spectrometer (Nicolet Instrument Corporation, WI, USA) in the range of 4000–400 cm^{-1} with a resolution of 2 cm^{-1}.

3.3 Tensile test

Mechanical properties of the fabricated dried fibers were evaluated using a Wance ETM 501 universal testing machine equipped with a 10 N load cell. To ensure consistency across all experiments, the samples were prepared by cutting the fibers to a standard length. To ensure homogeneous stress distribution, each sample was placed between two grips with a gauge length of 50 mm. The test was carried out in ambient conditions at a controlled crosshead speed of 3 mm min^{-1}. For testing the significance of the data, one-way ANOVA was used to test the data's significance, with $p < 0.001$ being deemed statistically significant.

3.4 Thermogravimetric analysis (TGA)

TGA was performed to prove the wetspun fibers were thermally stabilized using NETZSCH TG 209 F1 at a rate of 10 °C min^{-1}, while nitrogen was flushed at a rate of 100 mL min^{-1}.

3.5 X-ray diffraction analysis (XRD)

An X-ray diffractometer (XRD-SchimadzuXD-D1) with nickel-filtered Cu-K radiation at 30 kV and 45 mA was used to study the X-ray diffraction patterns of the fibers. The samples were scanned from 10° to 80° 2θ. The ratio of the area corresponding to the crystalline phase to the total area covered by the XRD curve was calculated using the provided formula to determine the degree of crystallinity for each sample.

$$\text{Crystallinity}(\%) = \frac{A_{\text{cr}}}{A_{\text{total}}} \times 100\%$$

where, the entire area under the XRD curve is represented by A_{total} and the crystalline area by A_{cr}.

3.6 Water absorption measurements

Water absorption capacity is a key parameter for evaluating the performance of wound dressings, as it influences moisture management and biological interactions. Each fiber was cut into uniform pieces of approximately equal dimensions to ensure consistency in measurements. The initial dry weight of each fiber sample was recorded using an analytical balance (W_{d}). Each sample was carefully dried at 37 °C for 24 hours to remove any residual moisture. The dried fiber samples were immersed in distilled water (DI water) at room temperature for 24 hours. The volume of water should be sufficient to fully submerge the samples. After 24 hours, the fiber samples were removed from the water, gently blotted with a tissue paper to remove excess surface water, and weighed (W_{w}). The formula for calculating water absorption measurements is given below;

$$\text{Water absorption}(\%) = \left(\frac{W_{\text{w}} - W_{\text{d}}}{W_{\text{d}}}\right) \times 100\%$$

3.7 Water vapor transmission rate (WVTR)

For measuring the samples' WVTR, fabrics were added one at a time to seal off the top of a beaker containing DI.[44,45] After being weighed, the beakers were stored in an airtight chamber at 37 °C. For ten days, the beakers' weight was recorded on a regular basis. This equation was used to measure WVTR;

$$\text{WVTR} = \frac{\Delta W}{tA}$$

where, t = time in days, A = test area, and ΔW = weight difference. Three iterations of the test were conducted, and average data with standard deviation were produced.

3.8 Whole blood clotting

To evaluate the entire blood clotting test, the blood clotting index (BCI) value was computed. The lower the BCI number, the more clotting power dressings have. Eventually, the supernatant of the precipitated blood clot has a lower absorbance value than blood cells and takes on a lighter color. The test was performed according to the previously published protocol.[46] The first step involved adding 100 mL of fresh whole blood to each sample and letting it sit at 37 °C for ten minutes. Then, 30 mL of DI was gradually added to the sample, and it was centrifuged for a minute and 3000 rpm was required. And the absorbance values at 540 nm were recorded using a UV-3100 spectrophotometer (J.P. Selecta, Spain). Blood was used as the control data without a sample. The blood clotting index (BCI) was computed using;

$$\text{BCI}(\%) = \frac{\text{Absorbance of blood with sample}}{\text{Absorbance of blood without sample}} \times 100\%$$

3.9 Hemolysis ratio as an indicator of biocompatibility

The direct contact method, as described in ISO 10993-4, was used to investigate the hemolysis ratio in order to prove that the generated fibers were hemocompatible.[47,48] In short, the erythrocytes were separated from the fresh human blood by centrifuging it at 3500 rpm min^{-1}. The resultant erythrocytes were suspended at a volume concentration of 2% (v/v) in saline. Next, the erythrocyte suspensions were incubated for one hour at 37 °C with the produced sample (10 mg), and then centrifuged for ten minutes at 3000 rpm min^{-1}. Using a UV-3100 spectrophotometer (J.P. SELECTA, Spain), the UV absorbance of the supernatant at 545 nm was determined. PBS was used as the negative control, and 1% Triton X-100 was used as the positive control. The samples hemolysis ratio (%) was determined using;

$$\text{Hemolysis ratio}(\%) = \frac{N_{\text{s}} - N_{\text{n}}}{N_{\text{p}} - N_{\text{n}}} \times 100\%$$

where, N_{s}, N_{p}, and N_{n} were the absorbance values of the sample, positive control group Triton X-100, and negative control group PBS, respectively.

3.10 RBC adhesion

According to the previously established protocol,[46,49] human whole blood was centrifuged at 1200 rpm for 10 minutes. To create a 10% (v/v) RBC solution with PBS, the RBCs were extracted from the platelet-rich plasma (PRP) and separated. For every sample weighing 10 mg, 200 μL of RBC solution was added. The combinations were then allowed to sit at 37 °C for one hour. After that, the samples were eluted with PBS three times. While the tightly attached RBCs were stabilized with 2.5% glutaraldehyde for two hours and stored in a freezer after dehydration with a series of 20, 40, 60, 80, and 100% ethanol for ten minutes each, the samples were air dried for 48 hours and finally investigated using FESEM.

3.11 *In vitro* PL release

A 25 mL solution of pH 7.4 PBS was added to the sample containing PL. The fluid was maintained at 37 °C to mimic wound conditions. The absorbance value at 278 nm was measured using a UV spectrometer after 18 days of data collection on absorbance. Every time, 3 mL of PBS was utilized and placed back into the primary solution. After the acquired data was analyzed, the cumulative release percentage was calculated.

$$\text{Cumulative PL release}(\%) = \frac{\text{Concentration}}{\text{Initial amount}} \times 100\%$$

The protein release kinetics were calculated by calculating the best fit of the cumulative percentage (%) drug release against time data to the Higuchi, Korsmeyer–Peppas, zero order, and first order equations.

$$Q_t = K_{\mathrm{H}} t^{(1/2)}$$

The drug release quantity at time (t) is denoted by Q_t, whereas the (Higuchian) release rate constant is represented by K_{H}.[50]

$$\ln\left(\frac{Q_t}{Q_\infty}\right) = \ln k + n \ln t$$

k is a constant that involves the geometry and structural properties of the film, n is the release exponent, Q_t is the amount of drug released at a specific time (t), and Q_∞ is the amount of drug present initially (Korsmeyer–Peppas).

$$Q_t - Q_0 = k_0 t$$

The quantity of medication released in time (t) is denoted by Q_t, the amount dissolved at time zero by Q_0, and the zero-order release rate constant by k_0.[51]

$$\ln\left(\frac{Q_\infty}{Q_1}\right) = k_1 t$$

Q_1 is the amount of drug left at time (t), Q_∞ is the initial total amount of drug present, and k_1 is the first order release rate constant.[52]

3.12 Molecular docking

Using AutoDock tools, the hydrogen bond prediction steps were examined. The alginate monomer (sodium glucuronate, MW 216.12 g mol^{-1}) and PEG monomer (ethylene glycol, MW 62.07 g mol^{-1}) three dimensional structures were acquired in sdf format from PubChem and used without conformational modification. The structures of PDGF, VEGF, and EGF were obtained in PDB format from the RCSB Protein Data Bank (PDB). These proteins were then prepared with AutoDock and saved in pdbqt format. Using the PyMol software, the ligand (SA–PEG monomer combination) was transformed to pdb format before being converted to pdbqt format. Since monomer units were docked rather than full polymers, standard AutoDock protocols are appropriate for this analysis. Lastly, LigPlus+ software was utilized to visualize whether hydrogen bonds were present between the ligands and the protein. These computational findings are preliminary and suggest potential interactions that require experimental validation.

3.13 *In vivo* diabetic wound healing experiment

These experiments were performed under the close supervision and authorization of Animal Care and Use Committee (ACUC), Department of Biomedical Engineering at Bangladesh University of Engineering and Technology (BUET) (approval number: 2024/BME/04). A total of 32 male Swiss albino mice weighing 35–40 g each were used in the investigation. When the mice were operated on, they were 8–10 weeks old. Mice were acquired from the International Centre for Diarrheal Disease Research, Bangladesh (ICDDR, B), and were kept in stainless steel cages with alternating cycles of light and dark. Both water and the same quantity of standard lab pellets were given to the animals. Before inducing diabetes, the mice were provided with 10% sucrose solution instead of normal drinking water for a period of two days. Subsequently, diabetes was induced by intraperitoneal administration of streptozotocin (40 mg per kg body weight), freshly prepared in citrate buffer (2.6 mg mL^{-1}), following 5 hours of fasting each day, for five consecutive days. Blood glucose concentrations were measured on days 0, 5, 10, and 15 using a glucometer (Gluco Dr SuperSensor Meter, Model AGM-2200) to verify successful diabetic induction. Mice were considered diabetic and eligible for inclusion in the experimental study when their blood glucose levels exceeded 150 mg dL^{-1} (8.3 mmol L^{-1}) and were significantly higher compared to the control group.[53] This threshold was selected as it is consistently above the normal physiological range for mice (approximately 4–7 mmol L^{-1}), confirming a sustained diabetic state suitable for evaluating impaired wound healing. A total of 32 mice were used across two independent cohorts ($n = 16$ per cohort). In each cohort, sixteen mice were randomly divided into four groups: control, SA-PEG-D-PL, SA-PEG-PL, and PL. For each time point (days 3, 7, 10, and 14), separate sets of mice from each group were designated for sacrifice and tissue collection. The progression of hyperglycemia in the cohort was as follows. On day 5 post-injection, the mean blood glucose level of the animals was 10.2 ± 2.1 mmol L^{-1}. By day 10, this had increased to 13.8 ± 1.9 mmol L^{-1}. On day 15, immediately prior to the wounding procedure, the mean blood glucose level was 14.5 ± 1.5 mmol L^{-1}. All 32 mice successfully met the inclusion criterion of >8.3 mmol L^{-1} on day 15 and were subsequently used in the wound healing experiments. Before beginning wound studies, all of the mice with severe hyperglycemia were given an intraperitoneal injection of ketamine hydrochloride at an optimal dose based on their body weight. Before being wound, the mice's dorsal hair was clipped off and disinfected with 70% ethanol. A typical wound was created using a biopsy punch that had a 1/4-inch (6.35 mm) diameter. Two wounds were created simultaneously on the left and right dorsal regions. These wounds were closed with sterilized SA-PEG-D-PL, SA-PEG-PL, and PL. The control group received no samples. The mice's incision sites were examined daily, and their regular postoperative feeding was maintained; no problems arose during this time. A camera was used to take pictures of the wound area at a predetermined height on the third, seventh, tenth, and fourteenth days.

Since a total of 32 mice were used across two independent cohorts, with $n = 4$ mice per group per cohort. After confirming consistency between cohorts, data were pooled, resulting in $n = 8$ mice per experimental group. These were distributed across four time points (days 3, 7, 10, and 14), yielding $n = 2$ mice per group per time point. Each mouse bore two wounds, providing four wounds per group per time point (2 mice × 2 wounds), these were not treated as independent biological replicates. During histological processing, one wound per group per time point was excluded due to technical artifacts (*e.g.*, tissue damage). All remaining evaluable wounds ($n = 3$) were included in quantitative analysis.

Quantitative measurements were first performed at the wound level and subsequently averaged per mouse to obtain one biological replicate per animal. Thus, the final biological sample size used for statistical analysis was $n = 2$ mice per group per time point. The mice were sacrificed on days three, seven, ten, and fourteen. The skin samples were preserved in 10% neutral buffered formalin. Additionally, the samples were embedded in paraffin and dehydrated in alcohol with varying concentrations. Sections of the implanted samples, each 4 μm thick, were cut out. Skin morphology and collagen deposition were observed using hematoxylin–eosin staining (H&E), periodic acid Schiff (PAS) staining, and masson's trichrome staining (MT), respectively, under the specification and conventional techniques. The healing process of diabetic wounds has been demonstrated to be exemplified by the reduction of the wound area over time. In particular, the wound regions on days 7 and 14 are highly predictive of wound healing.[54] Scar index and wound closure were determined using the following equations:

$$\text{Scar index} = \frac{\text{Scar area}}{\text{Adjacent normal dermal thickness}}$$

$$\text{Wound closure rate} = \frac{\text{Final wound area} - \text{initial wound area}}{\text{Initial wound area}} \times 100\%$$

3.14 Statistical analysis

Every experiment was run in triplicate, with each assay being independently repeated at least twice. In Minitab statistical software, the data were statistically examined using Tukey's multiple comparison test after one-way analysis of variance (ANOVA). The differences were considered significant at (*) $P < 0.05$, (**) $P < 0.01$, (***) $P < 0.001$.

4. Results and discussions

4.1 Fiber formation mechanism

In earlier research, wetspun SA fibers were effectively created and cross-linked using metal ions, although only G blocks were used.[55,56] In this study, a homogenous aqueous solution of SA and PEG is extruded through a spinneret into a calcium ion (Ca^{2+}) coagulation bath, illustrated in Fig. 1(A). Ionic cross-linking mostly takes place between the calcium ions and the guluronic acid (G) residues of alginate upon contact with the Ca^{2+} rich media, leading to the creation of fibers.[42] The gelation process is started by the quick ion-exchange between calcium ions (Ca^{2+}) in the coagulation fluid and sodium ions (Na^+) in the SA backbone. However, the kinetics of this exchange are altered by the presence of PEG. A more uniform and slow crosslinking process may result from inhibited Ca^{2+} transport into the fiber matrix caused by greater PEG concentrations. The fibers' mechanical performance and structural integrity are enhanced by this regulated gelation.

Here, hydroxyl groups (–OH) in PEG weakly interact with SA carboxyl groups or hydroxyl groups.[57] Although weak and non-covalent, hydrogen bonds are the main mediator of these interactions and can affect the surface striation and swelling behavior of the polymer network. A denser yet more elastic hydrogel structure can result from PEG's flexible chains filling in the gaps between the SA network's interstitial spaces. It adds to the biocompatibility and flexibility of the fibers, also lowering the viscosity of the SA solution and enhancing its spinnability.[58]

4.2 Catechol functionalization and PL immobilization

While dopamine based coating has been extensively utilized in various studies for improving bioactivity and surface adhesion, its application for platelet lysate immobilization is being demonstrated in this study for the first time. Which immobilize bioactive chemicals and enhance cellular interactions and therapeutic results. Since SA–PEG fibers are hydrophilic and lack particular cell binding sites, they naturally have limited cell adhesion capabilities. In order to solve this, hydroxyl groups are introduced *via* surface modification using NaOH, which increases surface reactivity, as seen in Fig. 1(B).[59] A polydopamine (PDA) layer is then created (Fig. S2) by the application of DA, which goes through oxidative self-polymerization. This PDA coating, which is abundant in catechol and amine groups and was inspired by mussel adhesive proteins, offers a flexible substrate for further functionalization.[60] PDA coatings are appropriate for biomedical applications since studies have shown that they promote cell proliferation and improve protein adsorption.[61] In order to ensure prolonged release and bioactivity, the PDA layer on the fibers helps immobilize PL by covalent bonding and physical adsorption. This immobilization technique has been demonstrated to improve cell differentiation, adhesion, and proliferation. A biomaterial with improved biological usefulness and mechanical integrity is produced by sequentially altering SA–PEG fibers with DA and NaOH, then immobilizing them with PL. These changes have been linked to better wound healing results, such as faster angiogenesis and re-epithelialization.

4.3 Characteristics of morphological structures

Fig. 2(A) shows the wetspun fibers' morphological characteristics. Since SA naturally has gel like and hydrophilic qualities, the surface of the SA only fiber appears rough. However, the absence of glycerol and PEG could lead to low mechanical strength and brittle fibers. SA's low stability when employed alone is highlighted by the apparent striation, which may be the result of shrinking after drying.[62] When PEG is added to the SA matrix, SA–PEG (5%), the fibers' surface becomes smooth moreover still exhibits fine striations. The two polymers exhibit partial miscibility, as evidenced by the presence of distinct yet

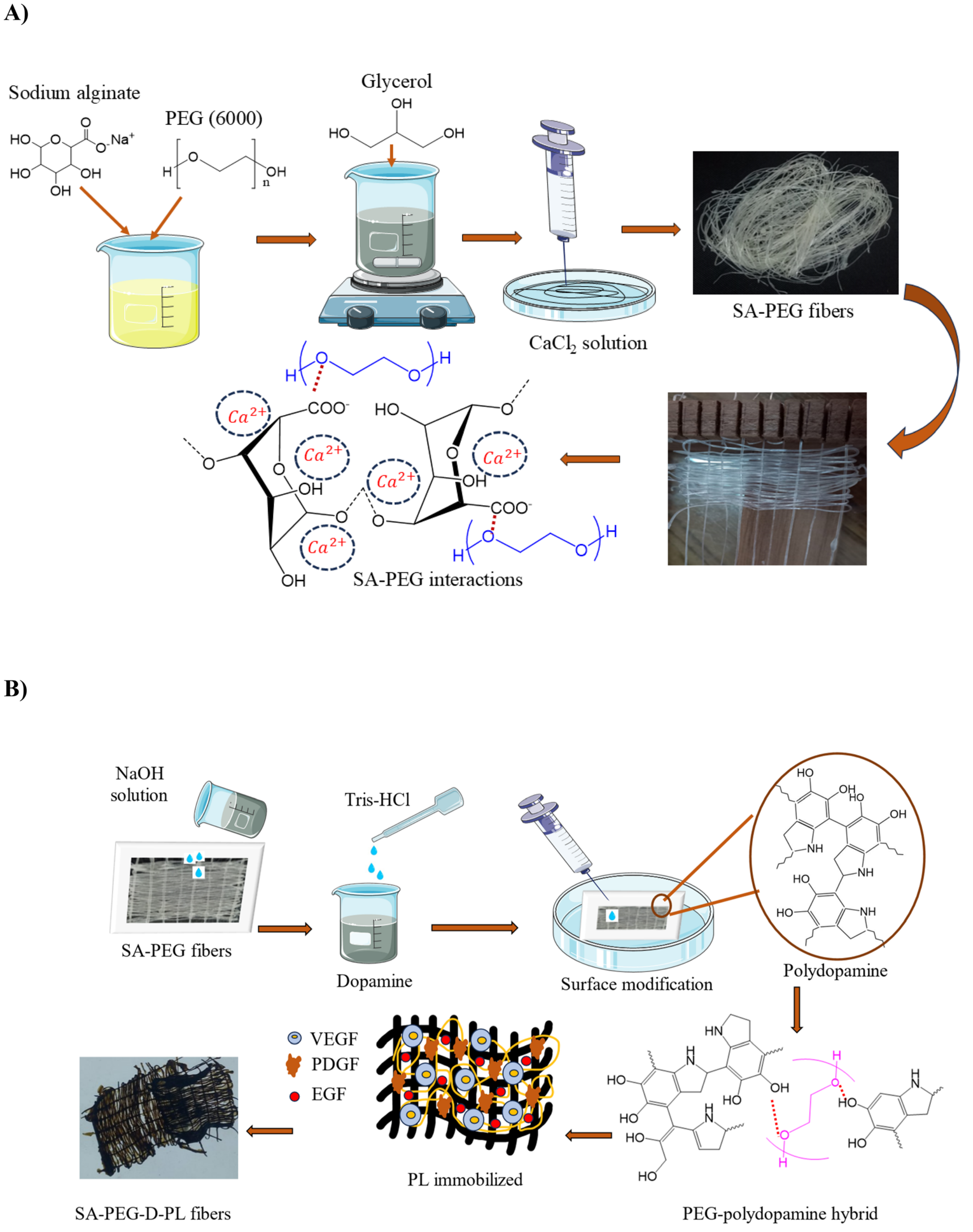

Fig. 1 (A) Schematic illustration of the wet spinning process of SA–PEG fibers. (B) Represents the surface modification steps: fibers are treated with NaOH to raise the pH, followed by polydopamine (PDA) coating. The PDA layer introduces catechol and amine groups that bind to the fiber surface through covalent and non-covalent interactions (hydrogen bonding, π–π stacking), facilitating the immobilization of proteins and growth factors.

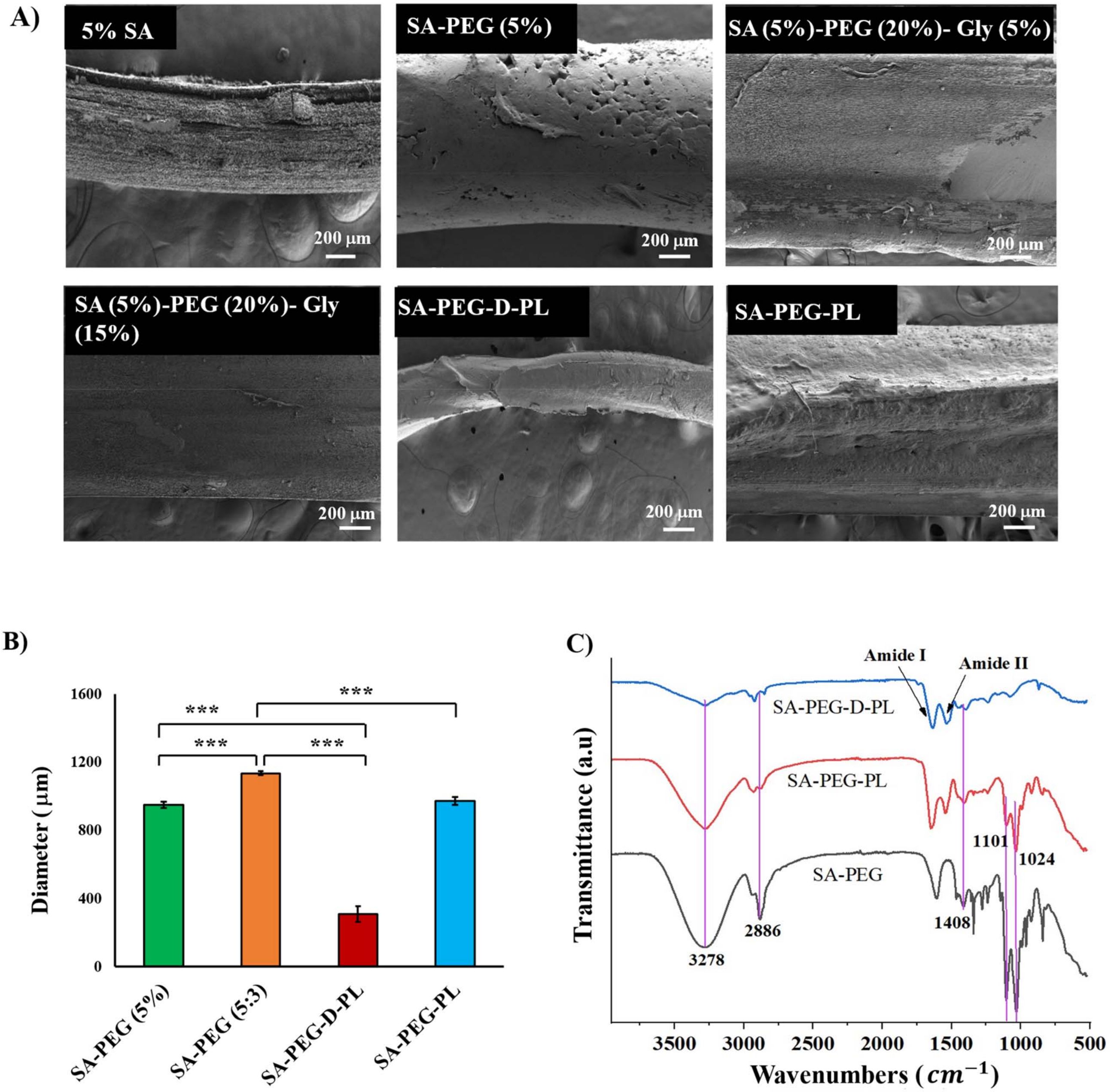

Fig. 2 (A) Surface morphology of the fibers. SA fiber's surface is noticeably rough, perhaps as a result of the quick solvent exchange. SA–PEG (5 : 3) shows a smooth fiber surface, further refined by the increased glycerol content, which likely enhances flexibility and reduces surface tension. SA-PEG-D-PL fiber demonstrates a layered morphology, attributed to the incorporation of PL and surface treatment that impacts the fiber structure. SA-PEG-PL sample displays slight surface irregularities. (B) Comparison of fiber diameters for SA–PEG (5 : 3), SA–PEG (5%), SA-PEG-D-PL, and SA-PEG-PL, the data were statistically examined using Tukey's multiple comparison test after one-way analysis of variance (ANOVA) (****p* < 0.001). (C) ATR-FTIR spectra of SA–PEG, SA-PEG-D-PL, and SA-PEG-PL showing successful immobilization of PL on the fiber surface.

interconnected fine structural features in the observed morphology. The brittleness of SA is offset by PEG's elasticity, which enhances the composite's mechanical qualities. The remaining surface imperfections suggest that the polymer matrix may not be completely homogenized by the PEG content. This composition is better suited for applications requiring both absorption and mild mechanical stability due to its flexibility and structured surface. In comparison to the earlier samples, SA (5%)–PEG (20%)–Gly (5%) fibers surface show improved smoothness and decreased striation depth with a higher PEG content and the addition of 5% glycerol as a plasticizer. Glycerol, SA and PEG combine to form a more cohesive polymer matrix. While the presence of glycerol improves flexibility and elasticity, the more compact surface indicates better mechanical stability. Applications needing both structural integrity and the capacity to adapt to uneven wound surfaces seem to be most suited for this composition.[63] When the glycerol concentration is increased to 15%, the fiber surface becomes smooth and dense, with a more uniform surface and reduced striation visibility.

The SA-PEG-D-PL formulation is particularly suited for applications requiring long-term wound coverage. A potential consideration for such smooth surfaces is that reduced topographical features could theoretically hinder the release of bioactive agents. However, this formulation is specifically designed to counteract this limitation. It incorporates bioactive proteins and growth factors that are released to stimulate cellular responses, including proliferation and migration, which are vital for tissue regeneration. The surface of the unmodified fibers, which have the same composition as the surface modified sample, is still compact and smooth shown in SA-PEG-PL. Because no extra microcracks are introduced Fig. 2(A), this intact surface morphology is significant because microcracks are known to act as stress concentration points that initiate mechanical failure, with studies reporting up to 25% reduction in tensile strength when such defects are present.[64] Therefore, the absence of treatment-induced microcracks in SA-PEG-PL suggests that avoiding chemical surface treatments preserves mechanical stability by maintaining a defect-free surface structure. While minimal surface imperfections can restrict passive protein adsorption and cell adhesion based on topographical cues alone,[65] this physical limitation is offset by the bioactive functionality imparted by the surface modification. The modification enhanced PL integration and uniform dispersion, enabling sustained release of bioactive factors. Consequently, the mechanism of cell–matrix interaction shifts from a reliance on surface topography to sustained biochemical signaling. This prolonged bioactivity actively promotes cell–matrix interactions essential for regeneration, even on a relatively homogeneous fiber surface. Compared to unmodified fibers, the synergistic effect of surface functionalization and PL incorporation markedly improves the wound healing efficacy of the modified fibers. Fig. 2(B) represents the variation of fiber's diameter. The diameters of SA–PEG (5 : 3) and SA–PEG (5%) are 1134.8 μm and 949.5 μm, respectively. SA–PEG (5 : 3) fibers were thicker than SA–PEG (5%) due to higher PEG content, which increased solution viscosity. SA-PEG-D-PL is often thinner approximately 309.7 μm, because surface treatments like NaOH or DA can lead to shrinkage or material loss due to dissolution or crosslinking, which compacts the fiber structure. On the other hand, SA-PEG-PL fibers caused slight swelling, increasing their diameter than surface modified fibers.

4.4 ATR-FTIR spectral analysis

Fig. 2(C) represents the ATR-FTIR analysis of the SA–PEG, SA-PEG-D-PL, and SA-PEG-PL, as well as the presence of bonding in the sample. Regarding pure SA fibers, two distinct absorption bands were found at 1608 cm^{-1} and 1408 cm^{-1}, which were ascribed to the symmetric and asymmetric stretching vibrations of the –COO group, respectively. It was determined that the bending vibration of C–O was responsible for the distinctive absorption band at 1101 cm^{-1} of PEG, whereas the bending and stretching vibrations of C–H were responsible for two absorption bands at 1340 cm^{-1} and 2886 cm^{-1}, respectively.[66] Also, the stretching vibration of O–H was the cause of the broad absorption band is also visible in 3421 cm^{-1}. However, from the ATR-FTIR spectra of SA–PEG blend fibers, for SA, the absorption bands at 1608 cm^{-1} and 1408 cm^{-1} moved to lower wavenumbers (1596 cm^{-1} and 1408 cm^{-1}) due to symmetric and asymmetric stretching of carboxylate (COO^{-}) groups. The N–H group's stretching vibration, which was normally bonded to the O–H group at 3421 cm^{-1}, was moved to 3278 cm^{-1}.[42,67] SA and PEG exhibit good molecular compatibility and strong intermolecular interactions, as evidenced by all those alterations. Peaks at 1540 cm^{-1} and 1451 cm^{-1} are associated with the amide II bending and stretching vibrations (NH and CN groups, respectively), whereas the absorption band at 1641 cm^{-1} is associated with the C═O stretching vibration of amide I. In the 1400–1200 cm^{-1} area, amide III-related NH bending vibration contributions are evident.[68,69] These indicate that PL is immobilized in both surface modified and unmodified fibers. SA-PEG-D-PL fibers show a peak at 3278 cm^{-1}, which corresponds to the O–H stretching vibration from hydroxyl groups present in both SA and PEG. Peak at 3278 cm^{-1} in case of modified sample, it would indicate that the –OH groups from SA–PEG are still present but possibly weakened due to the interaction with the surface modification that introduces overlap with a new peak near 3277 cm^{-1}, corresponding to the NH stretching vibration (amide A). It might not be as intense as in the unmodified sample, but it could still be visible. In contrast, the surface modified fibers demonstrate strong and more defined peaks for protein interactions. This indicates improved incorporation and strong interactions between the PL and the fiber structure.

4.5 Mechanical properties analysis

Tensile tests were performed on single dried fibers using a gauge length of 50 mm. Fiber diameter was measured using digital calipers during testing. The caliper measurement reflects the actual bulk diameter of the fiber used during tensile testing. The cross-sectional area was calculated assuming a circular cross-section $A = \pi\left(\frac{d}{2}\right)^2$. The diameters ranged from 560 μm to 980 μm, resulting in the following cross-sectional areas: SA–PEG (5 : 3) = 0.75 mm^2, SA–PEG (5 : 5) = 0.95 mm^2, SA–PEG (5%) = 0.44 mm^2, and SA-PEG-D-PL = 0.29 mm^2. The mechanical behavior of wetspun composite fibers composed of SA and PEG in a 5 : 3 mass ratio has been extensively studied along with other compositions (Fig. S3), to understand their tensile properties. The stress–strain curve of the SA–PEG (5 : 3) composite exhibits high strain-to-failure. This behavior is attributed to the increased chain mobility facilitated by the higher PEG content, which is a flexible polymer with a low glass transition temperature (T_g). By decreasing SA's interchain contacts and reducing ionic crosslinks and hydrogen bonds, the PEG chains increase elongation. Also in PEG, the dipole and van der Waals intramolecular forces predominate, which lessen stiffness. PEG dilution reduces the formation of crosslinks by the carboxyl and hydroxyl groups of SA, which are in charge of ionic and hydrogen bonding. A more flexible and deformable fiber is the end product. SA chains are penetrated by PEG macromolecular chains, giving the polymer matrix flexibility but decreasing its cohesive strength.[70]

As well as SA–PEG (5 : 3) shows 39.3 MPa young's modulus and 2.05 MPa tensile strength, highlighting its capacity to bear a certain amount of strain before cracking in Fig. 3(B). The flexibility of PEG's macromolecular chains, which lowers the density of hydrogen and ionic bonds in the SA matrix, is reflected in the lower modulus. Greater PEG concentration lowers the load bearing capacity while permitting ductile deformation.[67] SA–PEG (5 : 5) shows an optimal balance between stiffness and flexibility. Ionic crosslinks in alginate, such as Ca^{2+} bridges between guluronic acid residues, intensify and add to the material's stiffness. However, some of these interactions are broken by PEG, which reduces brittleness. To achieve intermediate mechanical qualities, the flexible chains of PEG partially soften the hard network of SA, forming a semi-interpenetrating network (semi-IPN).

Nevertheless, SA–PEG (5 : 5) shows a young's modulus of 177.2 MPa and a tensile strength of 1.7 MPa, indicating increased stiffness. SA adds stiffness; however, PEG content compromises the overall structural integrity. SA–PEG (5%) sample exhibits a sharp rise in stress, and a lack of significant PEG content limits flexibility. The macromolecular chains of SA are closely packed together, and the polymer matrix is dominated by strong ionic and hydrogen bonds. With a young's modulus of 291.7 MPa and a tensile strength of 22.7 MPa, SA–PEG (5%) exhibits superior mechanical strength and stiffness, albeit with decreased elasticity. On the other hand, DA and NaOH surface modification add catechol groups (also evident from Fig. S4) and enhance adhesion to PL proteins, strengthening intermolecular bonds. By interacting with SA and PEG *via*

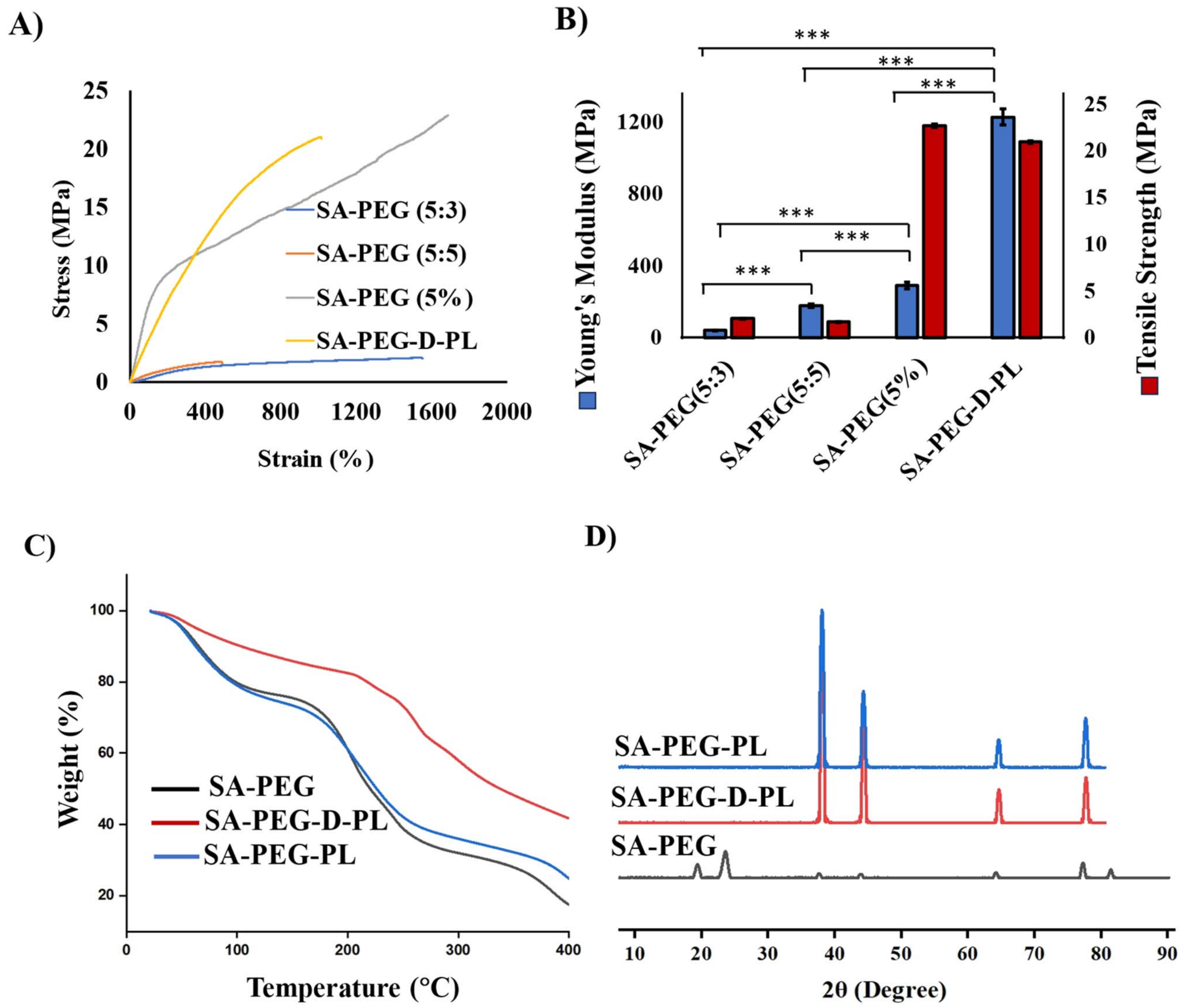

Fig. 3 (A) Stress–strain curve. (B) Young's modulus (MPa) and tensile strength (MPa) (C) TGA thermogram of SA–PEG (5 : 3), SA-PEG-PL and SM-PEG-D-PL (D) XRD pattern of SA-PEG, SA-PEG-D-PL and SA-PEG-PL. Mechanical testing demonstrates the reinforcing effect of PEG and the role of DA mediated surface modification in enhancing elasticity and strength. Thermal and structural analyses confirm improved thermal stability and intermolecular interactions in PL-loaded and surface modified fibers, indicating their potential suitability for wound healing applications.

hydrogen bonds and electrostatic forces, PL proteins (like PDGF, VEGF, EGF) can create a stiffer network. Through ionic interactions with the carboxyl groups of SA and the ether oxygen of PEG, the proteins from PL form a dense secondary network. Moreover, SA-PEG-D-PL shows young's modulus of 1228.5 MPa because of hydrogen bonding and adhesion to PL, increasing stiffness and tensile strength of 20.9 MPa. However, Thinner fibers exhibit higher Young's modulus due to enhanced chain alignment and reduced defects, and dopamine modification further reinforces the network, improving mechanical stability.[71–73] Overall, this structural stiffness provides support over the wound, while its strength ensures stability and longevity during handling and application.

4.6 Thermal properties evaluation

Fig. 3(C) demonstrates the thermal stability and decomposition behavior by the TGA plot. Compared to SA–PEG and SA-PEG-PL, the weight loss in the SA-PEG-D-PL sample is more gradual throughout the first decomposition stage (150 °C to 250 °C). Main stage of degradation (250 °C to 400 °C), degradation for the SA-PEG-PL starts earlier (about ~240 °C) than for the surface modified sample (around ~270 °C). This suggests that altering the surface postpones the start of deterioration. SA–PEG and SA-PEG-PL show nearly total breakdown at high temperatures 400 °C, although the surface modified sample keeps a sizable amount of its weight.[74] Thermally stable compounds could be the cause of the surface modified sample's greater residue weight. The onset temperature is somewhat shifted by protein interactions when PL is added to SA-PEG-PL, however the thermal stability is unaffected.[75] Conversely, DA surface modification probably results in the formation of covalent connections between DA molecules and SA–PEG chains, which raises the crosslink density. Additionally, proteins and GFs can help reinforce the polymer matrix. Moreover, it shows that the modified sample produces more thermally stable carbonaceous char, which may be related to the integration of DA with PEG and SA and their polymerization. Notably, the delayed onset of breakdown and higher residual weight of the SA-PEG-D-PL indicate that it has better thermal stability than the unmodified and SA–PEG samples.

4.7 XRD analysis of structural crystallinity

Fig. 3(D) shows the XRD patterns of 3 samples SA–PEG, SA-PEG-D-PL and SA-PEG-PL. We can see the peaks at $2\theta = 13.5°$, 22.5° and 32°, these correspond to the (110), (200), and (211) planes, which are produced by the crystalline areas of SA that are created by intermolecular hydrogen bonds in its polymer chains. PEG contributes extra peaks at 19° and 23°, which are often connected to the (120) and (112) planes and reflect its crystalline structure.[76] The inclusion of PL improves the crystallinity of PEG, as seen by the sharpening of the peaks at 19° and 23° in the SA-PEG-PL sample. Although the SA peaks at 13.5°, 22.5°, and 32° are still discernible, their relative intensities vary, maybe as a result of interactions with growth factors and proteins. The relative intensities of SA are still present in SA-PEG-D-PL, but they are altered by PL immobilization. Peaks at 31°, 40°, and 45° are more intense and sharper than those at SA-PEG-PL; this could be because of the surface functionalization process.

The crystallinity percentage and crystalline size of the samples were also calculated to further evaluate the impact of PL immobilization and catechol functionalization. SA–PEG showed 34.2% crystallinity with a crystalline size of 10 nm, reflecting its semi-crystalline nature. Upon PL addition, crystallinity increased to 36.6% and size to 17.3 nm in SA-PEG-PL, indicating improved molecular ordering due to interactions with PL components. Similarly, SA-PEG-D-PL exhibited 35.8% crystallinity and a similar crystal size of 17.3 nm, suggesting that DA modification promotes crystal growth, possibly by facilitating surface interactions, despite minor structural disruptions. Overall, both PL and surface modification enhance crystalline organization within the polymer matrix.

4.8 Water absorbency

Fig. 4(A) represents the water absorbency of three different fabrics: SA–PEG, SA-PEG-D-PL, and SA-PEG-PL. The water absorbency of SA–PEG is the lowest (around 14%). The untreated fibers' compact structure restricts their surface striation and water retention capacity. Conversely, the SA-PEG-D-PL fibers exhibit a significant increase in water uptake of approximately 719%, which can be attributed to the chemical alterations induced by surface functionalization, leading to enhanced hydrophilicity. By drawing and holding onto water molecules *via* hydrogen bonds and dipole interactions, as hydrophilicity improves water absorbency also evident from swelling and degradation properties Fig. S5. Strong interactions between hydrophilic groups like hydroxyl (–OH) and carboxyl (–COOH) and water enable the material to absorb and retain more moisture.[62] On the other hand, SA-PEG-PL absorbs about 47% water, due to the addition of growth factors and hydrophilic proteins from PL, which interact with water molecules and improve the material's moisture retention capacity.

4.9 Water vapor transmission rate

Fig. 4(B) shows WVTR of three samples SA–PEG, SA-PEG-D-PL, and SA-PEG-PL. SA–PEG shows the greatest WVTR among all, indicating a more permeable structure that allows water vapor to pass through. A high WVTR can help avoid excessive fluid buildup, but it can also cause the wound to rapidly dehydrate, which is not ideal for long term wound healing applications like diabetic wounds. The dressing with a WVTR of roughly 2028.3 g per m^2 per day might preserve the ideal moisture content for fibroblast and epidermal cell growth and function.[77] Additionally, it was shown that a WVTR rate of 2000–2500 g per m^2 per day would supply a sufficient amount of moisture without running the danger of desiccation.[78] A further decline in WVTR of about 2297.3 g per m^2 per 24 day was seen in the SA-PEG-D-PL sample. This implies that the surface modification process adds to other modifications in the fiber network, which could change the material's surface striation and make it more hydrophilic.[79] Polydopamine surface coatings are known to produce an adhesive, hydrophilic layer that improves water affinity and

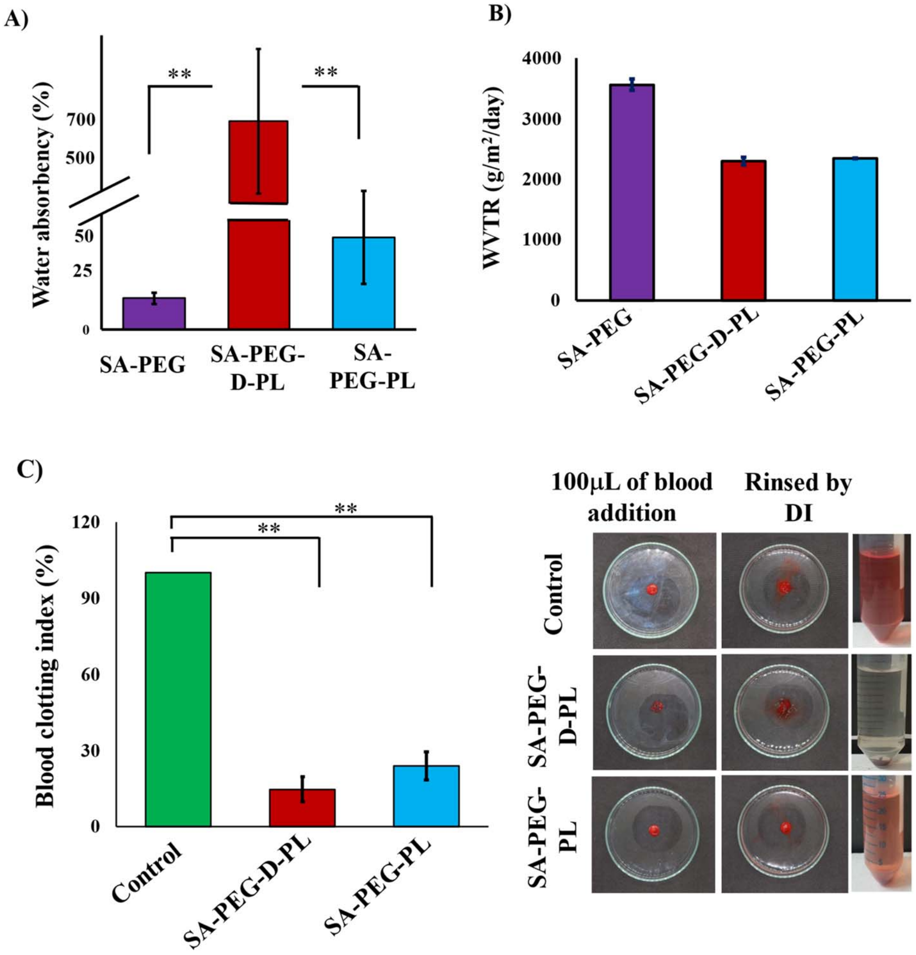

Fig. 4 Evaluation of (A) water absorption capacity, (B) water vapor transmission rate (WVTR), and (C) blood clotting index (BCI) of SA–PEG based fibrous dressings. SA-PEG-D-PL exhibited significantly enhanced water absorption and reduced BCI, indicating improved exudate handling and hemostatic performance. Statistical significance is indicated as $p < 0.01$ (**) and $p < 0.001$ (***). The exceptional water absorption ability of SA-PEG-D-PL highlighted its potential to sustain a moist wound microenvironment that promotes healing. In comparison to the control, SA-PEG-D-PL significantly lowers BCI, confirming improved blood interaction and clot promoting capacity.

surface free energy.[80] This altered interface may improve the material's ability to retain moisture by reducing vapor driven moisture loss. However, compared to the pure SA–PEG sample, the SA-PEG-PL sample, which contains PL but does not have surface modification, showed a lower WVTR of approximately 2343.3 g per m^2 per day. The presence of proteins and bioactive compounds from the PL may have an impact on the polymer network by enhancing moisture retention and marginally decreasing fiber permeability, and for this, WVTR has decreased. Water vapor permeability may decrease as a result of a dense or more structured arrangement created by the interaction of PL components with the polymer matrix. This denser arrangement creates a tortuous path for water vapor diffusion, a well-established mechanism where fillers physically hinder vapor transport by forcing water molecules to travel longer pathways through the polymer matrix.[81]

4.10 Whole blood clotting

Fig. 4(C) shows the hemostatic property of fibers. The SA-PEG-D-PL group exhibited a BCI of 14.6%, whereas the SA-PEG-PL group showed a higher BCI of 23.8%. The reduction in BCI reflects an enhanced anticoagulant property of the surface modified fibers, suggesting that both dopamine mediated surface functionalization and the incorporation of PL contribute to decreased blood clot formation. The surface modified sample's rapid rate of expansion, and potent water absorption capability allow it to absorb blood water rapidly, encourage blood cell adhesion and aggregation, and exhibit good coagulation ability *in vitro*. Rapid hemostasis is made possible by the fibrous network that supports fluid exchange and cell infiltration and a high rate of expansion, which improves red blood cell adsorption capacity.[82] Compared to the SA-PEG-D-PL group, the BCI% of the SA-PEG-PL group is marginally greater, approximately 23%. This suggests a moderate level of anticoagulant activity. Because PL releases bioactive substances such as growth factors and cytokines, which alter clotting mechanisms and improve anticoagulant qualities, it raises the BCI. It makes the substance more blood compatible by lowering the production of clots.

4.11 Hemocompatibility evaluation

Fig. 5(A) represents the hemolysis ratio to evaluate the blood compatibility of the fibers. The degree of red blood cell fracture and disintegration caused by the sample coming into contact with blood is indicated by the hemolysis ratio.[83] During hemolysis, red blood cells (RBCs) are destroyed, and the two surrounding environments contain free hemoglobin. Consequently, a lower hemolysis ratio is linked to better blood compatibility. According to ASTM guidelines, a material's permissible hemolysis ratio for medical use must be less than 5%.[84] SA is more likely to interact with RBC membranes because of its larger molecular weight, which may lead to a higher rate of cell lysis.[85] The results showed that all of the dressings with PL had hemolysis rates less than 5%. As a result, SA-PEG-D-PL scaffolds were found to have a very good blood compatibility level. Plasma proteins (albumin, fibrinogen) and growth factors (PDGF, VEGF, and TGF-β) are abundant in PL. These proteins can reduce direct interaction between the biomaterial and RBC by attaching themselves to the surface of the biomaterial and creating a barrier. This reduces RBC damage and hemolysis from chemical or mechanical causes. DA may induce severe hemolytic damage due to its high charge density of free amino groups, which causes excessive interaction with erythrocyte membrane components and destroys the membrane structure.[74] The combination of NaOH and dopamine treatment likely enhances the hydrophilicity of the fibers. Increased hydrophilicity reduces nonspecific protein adsorption and cell adhesion, thereby minimizing RBC damage.[86,87] In contrast, the SA-PEG-PL samples may exhibit lower hydrophilicity, which could promote stronger interactions with blood cells and a higher risk of hemolysis. These findings emphasize the crucial role of surface modification in improving the blood compatibility of the fibers.

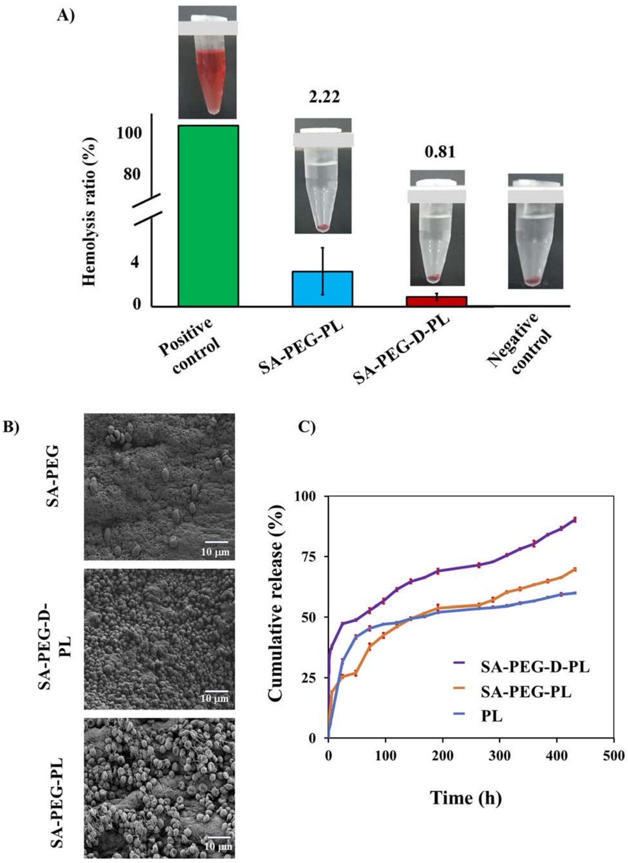

Fig. 5 (A) Hemolysis ratio, (B) RBC adhesion, and (C) *in vitro* cumulative release of PL from fibrous dressings. Comparing SA-PEG-D-PL to SA-PEG-PL, the hemolysis ratio was much lower (0.81%), both staying far below the 5% blood compatibility criterion. Red blood cell attachment on SA-PEG-D-PL is dense and consistent, according to SEM measurement of RBC adhesion; this indicates a favorable blood–material interaction, while SA–PEG showed scant cell presence. However, over the course of 18 days, PL was shown to have a sustained release; SA-PEG-D-PL showed the largest cumulative release, indicating that it may have long term therapeutic activity in wound healing applications.

4.12 RBC adhesion

Fig. 5(B) shows the hemostatic mechanism to examine the surface adhesion and morphology of blood cells and platelets.[88] The SA–PEG surfaces exhibit minimal fibrin network formation and limited blood cell adhesion, indicating weak interactions with blood components. This suggests inadequate tissue adhesiveness and suboptimal hemostatic performance. Blood cell adhesion is significantly increased in SA-PEG-D-PL samples, where cells are closely packed throughout the substance. Surface changes like DA coating, which increase tissue adhesiveness and speed up the coagulation process, are probably the cause of this improved connection. A thick fibrin network is seen in SA-PEG-PL samples, which capture a lot of blood cells. The fibrin structure holds the cells in place, suggesting better hemostatic qualities than the pure SA–PEG. This is probably because PL was added. Comparing the interaction to the surface modified samples, it is less consistent. The DA coating's increased adhesiveness promotes stronger RBC interaction and noticeable deformation during adhesion. Which causes the shape shift of RBCs on the surface modified sample. However, this deformation was not associated with cell rupture, and it was consistent with lower hemolysis. On the SA–PEG surface, erythrocytes retained their characteristic biconcave shape and were sparsely adhered, indicating minimal interaction with the surface. In contrast, SA-PEG-PL and SA-PEG-D-PL exhibited significantly higher erythrocyte adhesion, with a noticeable morphological transition of RBCs from their native biconcave structure to spherical forms. This transformation is indicative of erythrocyte activation, often associated with the development of stable clots and enhanced hemostatic performance.[89] As well as numerous phenolic hydroxyl groups found in DA in SA-PEG-D-PL can interact with plasma fibronectin and erythrocytes and platelets adhesion to cause platelet activation.[86]

4.13 Release of PL from fibrous wetspun

Fig. 5(C) represents the cumulative release (%) over 18 days. The analytic release data were examined using the zero order, first order, Higuchi, and Korsmeyer–Peppas models in order to comprehend the manner of drug release from three samples.

The primary determinant of the best-fitting model is the correlation coefficient (R^2), Fig. S6. Comparing the three samples to other models, it was discovered that the Korsmeyer–Peppas model's R^2 (0.99) was higher. Based on these findings, it is likely that the Korsmeyer–Peppas model governs the release kinetics of these dressings.[90] PL exhibited a rapid initial release, reaching approximately 50% cumulative release within the first 50 hours, followed by a slower phase at around 60% by 432 hours. This burst release is likely due to the absence of a regulating matrix, allowing rapid diffusion of PL into the surrounding medium. In contrast, the SA-PEG-PL sample showed a moderate initial release of about 30% in 50 hours and a gradual increase to nearly 70% by 432 hours, indicating the matrix's ability to act as a diffusion barrier and sustain release over time. The SA-PEG-D-PL sample demonstrated the most controlled and extended release profile, reaching around 35% at 50 hours and nearly 90% at 432 hours, suggesting that dopamine functionalization further enhanced the matrix's capacity for prolonged and regulated release. The surface alteration, which improves hydrophilicity and promotes better lysate diffusion, is probably the cause of the increased release when compared to the unmodified sample.[91,92] A more open and interconnected matrix structure makes the matrix's channels bigger or more linked, which facilitates the PL's easier diffusion. Water absorption is improved by increased hydrophilicity, which also causes the matrix to swell and weaken its structure, which facilitates PL release. When combined, these characteristics lower diffusion barriers, resulting in increased and prolonged PL release.

4.14 Molecular docking

The interaction between SA–PEG with PL, which contains important GFs, such as VEGF Fig. 6(A), PDGF Fig. 6(B), and EGF Fig. 6(C), was assessed using molecular docking experiments. Both panoramic and two-dimensional views of the discovered docking conformations shed light on the binding behavior and possible bioactivity of these complexes. The panoramic views display several spatial configurations and show the general binding direction of each growth factor within the SA–PEG matrix. Specific non-covalent interactions that support the stability of the complexes, such as hydrophobic contacts, electrostatic interactions, and hydrogen bonds, are further clarified by the 2D interaction maps. The binding affinities of the three growth factors varied, VEGF exhibiting −6.5 kcal mol^{-1}, PDGF −7.2 kcal mol^{-1}, and EGF demonstrating −6.9 kcal mol^{-1}. The varying binding energies suggest differences in the complexes' stability and molecular recognition. PDGF's greater binding affinity could be explained by the complex being predicted to have more hydrogen bonds, electrostatic interactions, and hydrophobic contacts. A more negative binding energy suggests a stronger and more stable interaction between the biomaterial and the growth factor. The docking result suggests that PDGF may have a more favorable and stable integration within the SA–PEG matrix compared to the others. The higher binding energy of PDGF can be attributed to the formation of multiple stabilizing interactions *in silico*.

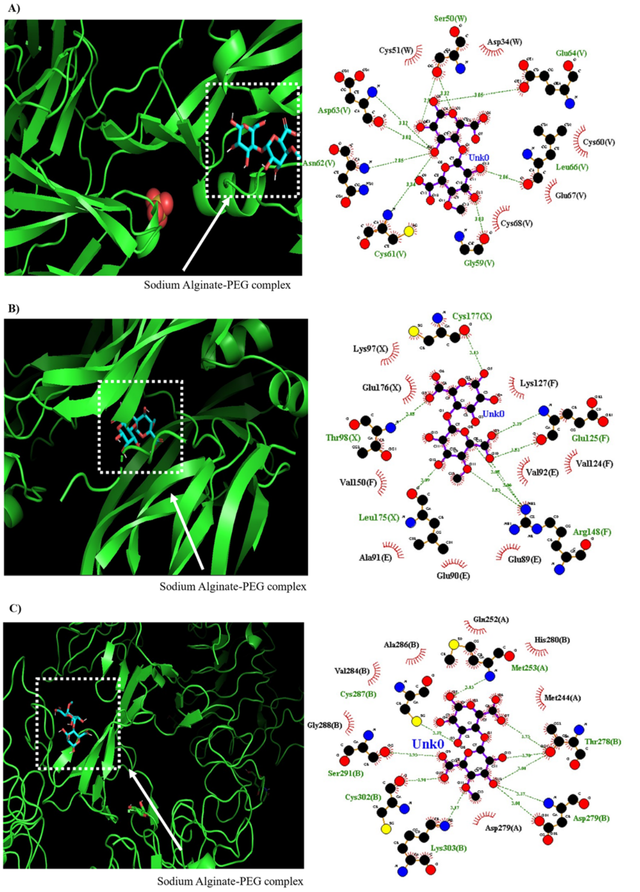

Fig. 6 Molecular docking analysis of hydrogen bonding between sodium alginate–PEG with (A) VEGF, (B) PDGF, (C) EGF which are the key components of PL. The docking simulations reveal specific binding conformations and interaction sites, suggesting potential affinity of sodium alginate–PEG for stabilizing and immobilizing these growth factors within the fiber matrix.

The strong binding of PDGF may be attributed to the presence of multiple hydrogen bonds and electrostatic interactions, likely involving positively charged residues such as Arg and Lys engaging with the carboxyl groups of SA. These molecular interactions could enhance physical encapsulation and promote controlled release, aligning well with observed *in vitro* release trends. The panoramic and 2D interaction views confirmed structural compatibility and revealed how the growth factors were spatially oriented within the polymeric network.

4.15 *In vivo* experiment

Fig. 7(A) represents the SA-PEG-D-PL fibers' ability to repair wounds *in vivo* compared to that of PL in mice. The sequential photos of the wounds were taken at days 0, 3, 7, 10, and 14. As can be seen from Fig. 7(A), SA-PEG-D-PL improved wound healing. Even after 14 days, as anticipated, the wound could not be closed by natural healing. Furthermore, when SA-PEG-PL and PL were utilized to treat wounds, they did not heal completely. Nevertheless, improved wound healing was evident from day 7 when evaluating the effectiveness of SA-PEG-D-PL.

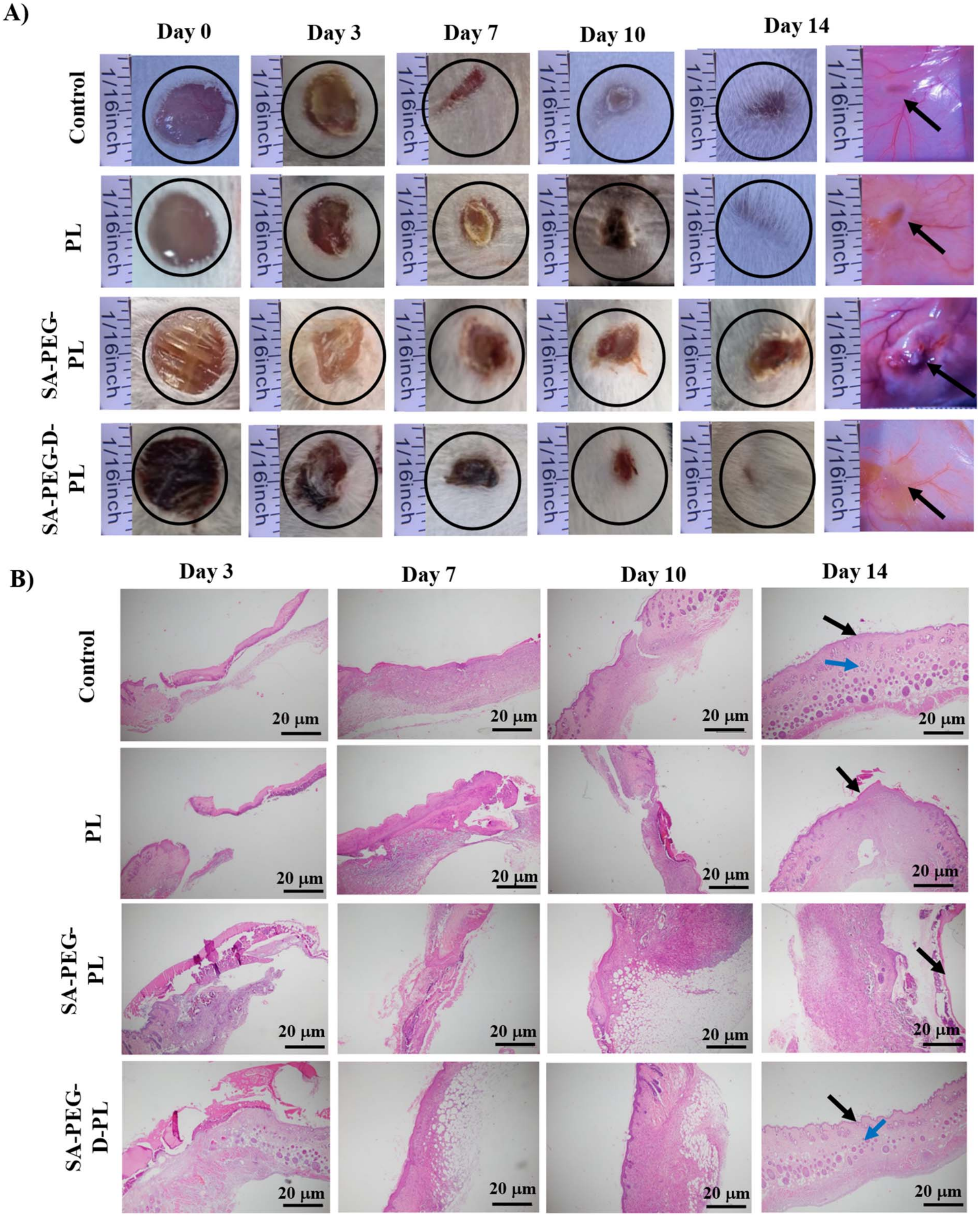

Fig. 7 (A) Images of wounds treated by control, PL, SA-PEG-PL, and SA-PEG-D-PL at different time points of 0, 3, 7, 10, and 14 days, also show dermoscopic images of wound beds after day 14. SA-PEG-D-PL promoted better wound healing than the other samples. (B) Represents H & E-stained tissue sections that ensure re-epithelialization and tissue regeneration. Black arrows represent re-epithelialization, and blue arrows represent neovascularization.

After 14 days, wound traces were found in all samples except for SA-PEG-D-PL. Fig. 7(A) also shows the wound beds. However, in SA-PEG-PL and PL, there were indications of tissue abnormalities and wounds surrounding the treated area.

To investigate the impact of SA-PEG-D-PL on wound healing and its many characteristics, excised wounds were stained with H & E, MT, and PAS. The excised wounds were examined for inflammatory cells, neoangiogenesis (Fig. S7), scar index, re-epithelialization, and epithelial gap, among other wound healing indicators. On day 3, wounds treated with SA-PEG-D-PL and SA-PEG-PL showed a strong inflammatory response with neutrophils, macrophages, and lymphocytes present, indicating an early immune response required for wound cleaning. However, by day 7, a direct comparison of inflammatory cell counts Fig. 8(A) reveals that SA-PEG-D-PL treated wounds had dramatically fewer inflammatory cells than SA-PEG-PL and control group, indicating a quicker resolution of inflammation. Prolonged immune activation and chronic inflammation were suggested by the control group's highest inflammatory response, which persisted until day 14. A continuous layer of epidermis was developed by day 7, indicating active migration and proliferation of keratinocytes. The well-stratified epidermis of SA-PEG-D-PL by days 10 and 14 demonstrated full tissue remodeling and epithelialization. Direct comparison of re-epithelialization Fig. 8(B) shows that SA-PEG-PL treated wounds had slower epidermal coverage with visible gaps even at day 10, while PL-only and control groups showed only partial closure by day 14. With partial closure at day 14, the PL-only and control groups showed the slowest epidermal recovery, underscoring the limited effectiveness of PL by itself in fostering epidermal regeneration. The SA-PEG-D-PL group had the highest levels of collagen deposition and fibroblast proliferation, which are essential for ECM remodeling. Collagen fibers were closely packed by day 10, which suggested improved tissue strength and matrix remodeling. On the other hand, wounds treated with SA-PEG-PL showed considerable fibroblast activity, but the extracellular matrix remained loosely organized, indicating slower matrix organization.

There was insufficient structural support for wound contraction in the PL-only group, as evidenced by the limited

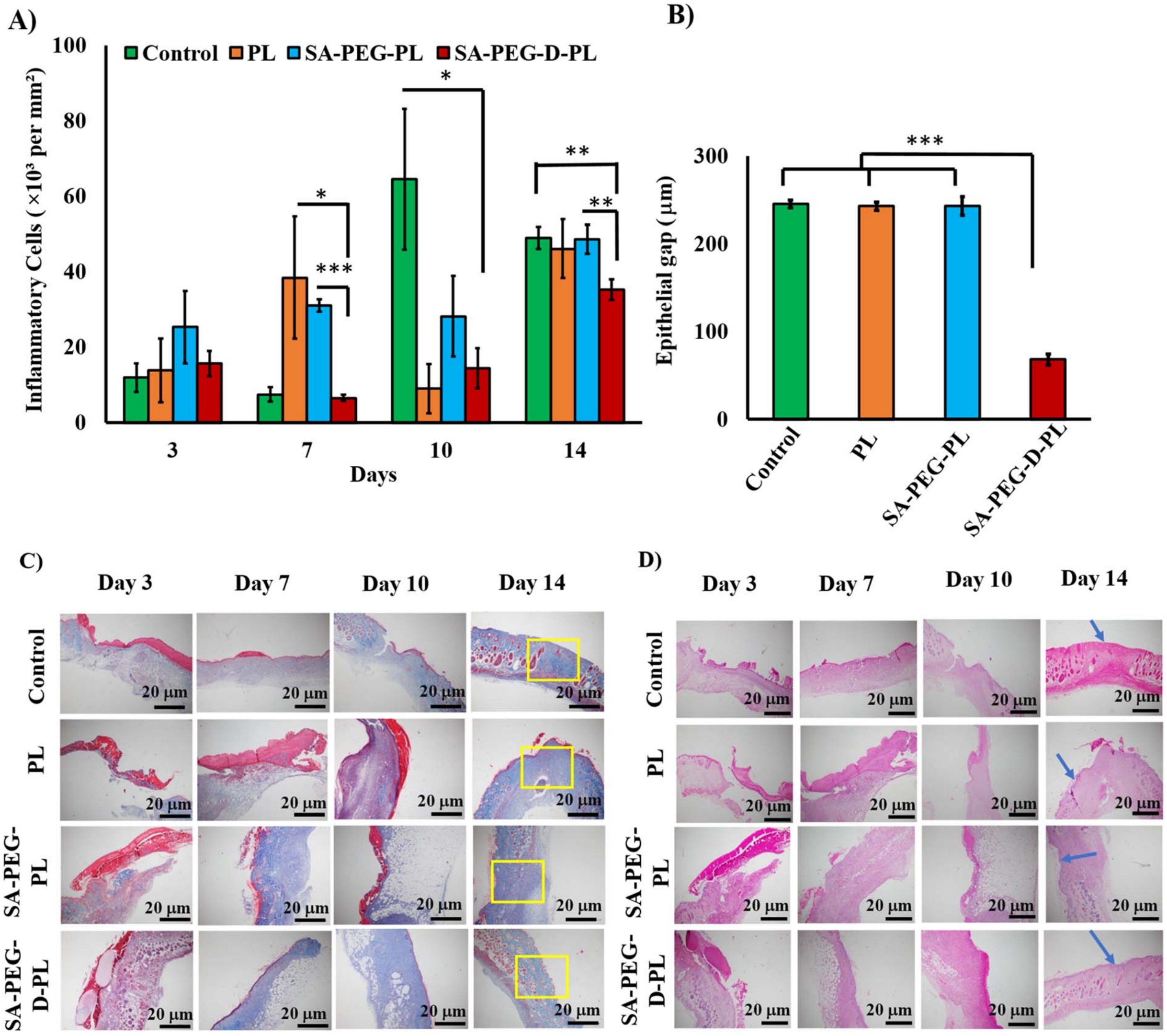

Fig. 8 (A) The number of inflammatory cells per mm^2 was calculated on days 3, 7, 10, and 14 for SA-PEG-D-PL, SA-PEG-PL, PL, and control. (B) The epithelial gap of all four wounds after three days. After three days, the gap of the wound treated by SM-PEG-D-PL significantly decreased compared to other samples. (C) MT staining, the yellow area represents collagen deposition in the wounded area. (D) PAS staining of wounds in all the cases on days 3, 7, 10, and 14. Significant differences are indicated by * ($p < 0.05$), ** ($p < 0.01$), *** ($p < 0.001$).

fibroblast proliferation and ECM deposition in the control group. Early and continuous blood vessel development was seen in the SA-PEG-D-PL group by day 7 and persisted until day 14. This implies that the bioactive surface alteration enhanced cellular interactions and GF retention, hence encouraging vascular regeneration. In contrast to the control group, which showed poor vascularization, the SA-PEG-PL and PL groups showed confined angiogenesis, which may have limited the delivery of nutrients and oxygen to the regenerated tissue. This study shows that SA-PEG-D-PL fibers promote quicker inflammation resolution, re-epithelialization, ECM remodeling, and angiogenesis, all of which greatly improve wound healing.

Fig. 8(C) represents the samples' MT staining. Information about collagen deposition in the cutaneous region is given. A better structured collagen network with more deposition was seen in the SA-PEG-D-PL group on day 7, indicating improved ECM remodeling and wound healing. Conversely, the PL and SA-PEG-PL groups displayed less structural organization and moderate collagen formation. The control group had uneven tissue architecture and little collagen deposition, which suggested that wound healing was delayed. By day 14, the scar areas in the control group were more prominent, whereas the SA-PEG-D-PL group exhibited reduced scar formation in Fig. 9(B), indicating superior wound healing. The scar index comparison

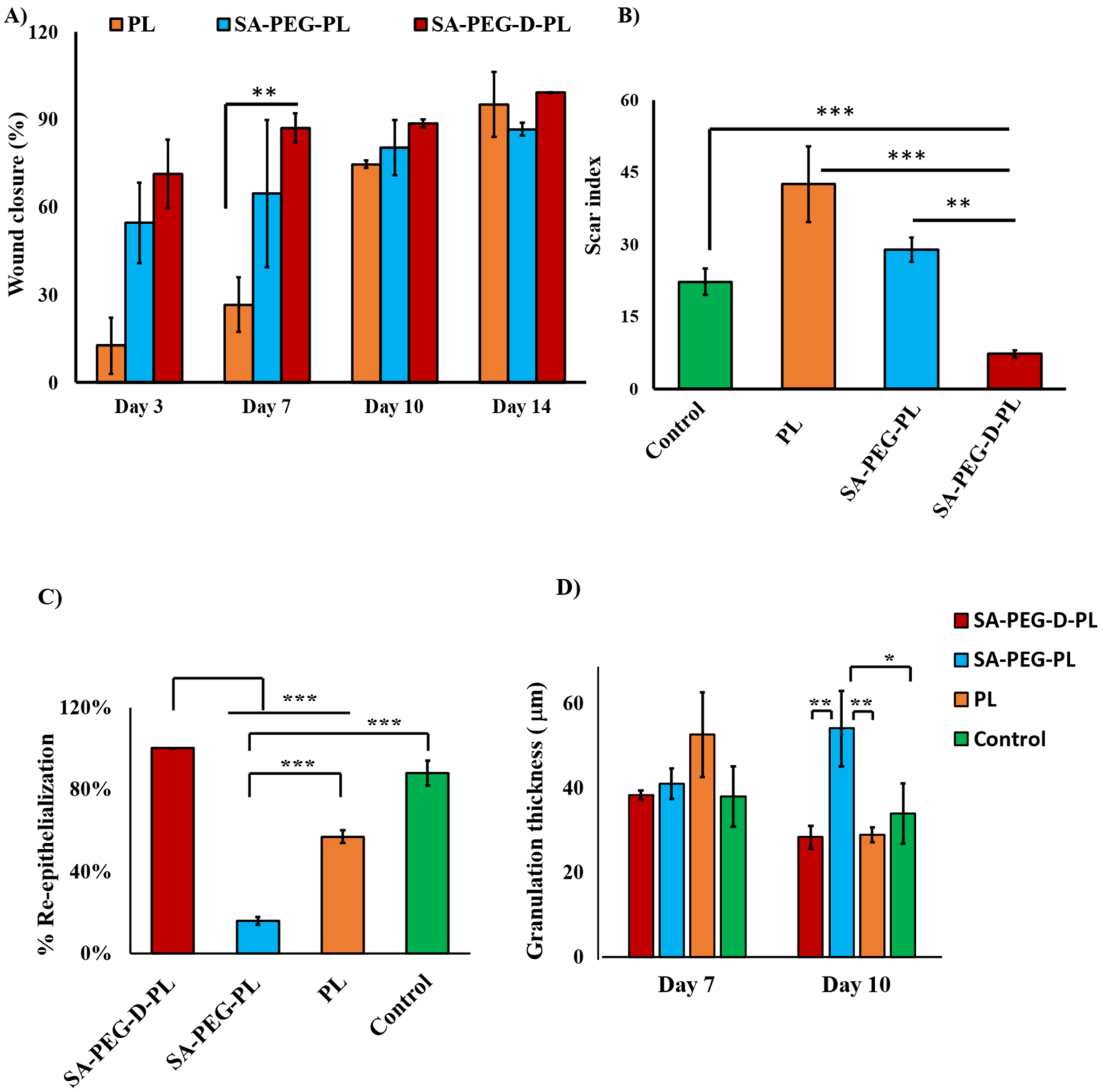

Fig. 9 (A) Wound closure (%) on 3, 7, 10, and 14 days. (B) Scar index of all four wounds after 14 days, where the scar area was the smallest in the case of SA-PEG-D-PL. Compared with the control and other treatment groups, the SA-PEG-D-PL group demonstrated noticeably improved wound contraction over time. Also showed enhanced skin regeneration and a discernible decrease in scar tissue. (C) % Re-epithelialization on day 10. (D) granulation tissue thickness (µm) in diabetic wounds treated with different formulations on days 7 and 10. Statistical analysis was performed using one-way ANOVA with Tukey's; exact p-values are provided in the Results section (*$p < 0.05$, **$p < 0.01$, ***$p < 0.001$).

Fig. 9(B) directly shows that SA-PEG-D-PL (7.3) is significantly lower than unmodified fibers (SA-PEG-P) (29), PL (42.6), and control (22). Additionally, epithelial thickness measurements suggest that the SA-PEG-D-PL group facilitated better re-epithelialization compared to the other groups. The basement membrane rebuilding is a crucial factor because it divides the dermis layer beneath the epidermis.[93] Several crucial proteins, including collagen IV and laminin, are found in the dermis layer, which also regulates both dermal and epithelial cells.[94]

On day 7, the control group's basement membrane was absent in all the wound sites in Fig. 8(D), indicating a break in the epidermis-dermis link. With partially regenerated BM connecting the epidermal and dermal layers, the SA-PEG-D-PL and SA-PEG-PL groups, on the other hand, demonstrated superior basement membrane integrity. However, direct comparison on day 14 reveals that only SA-PEG-D-PL showed a well-compacted, continuous basement membrane at the wound center, while SA-PEG-PL continued to exhibit persistent gaps between epithelium and dermis. Nonetheless, the SA-PEG-PL group continued to exhibit persistent gaps between the epithelium and dermis, whereas the SA-PEG-D-PL group showed a more continuous basement membrane, suggesting better epithelial regeneration. All groups showed more formed basement membrane structures by day 14, with the wounds treated with SA-PEG-D-PL showing a well-compacted basement membrane, especially at the wound center. Furthermore, this group's epidermis showed early ridge formations, which signaled the papillary dermis's appearance. In contrast, the other groups' epidermis remained comparatively flat. Additionally, follicular structures were visible in the wounds treated with SA-PEG-D-PL, although the follicular structures of the SA-PEG-PL group were restricted. In the wounds treated with SA-PEG-D-PL, neoangiogenesis was seen as early as day 3, indicating faster vascular regeneration. All groups' blood vessel creation was measured by day 7; however, the wounds treated with SA-PEG-D-PL showed the highest levels of angiogenesis, most likely as a result of the bioactive environment promoting healing. Angiogenesis had decreased by day 14, which was consistent with the typical course of wound healing. According to these results, SA-PEG-D-PL plays a promising role in improving diabetic wound healing by markedly enhancing angiogenesis, follicular restoration, papillary dermis creation, and basement membrane regeneration.

At day 10, the SA-PEG-D-PL and SA-PEG-PL groups exhibited significantly higher re-epithelialization percentages compared to the PL and control group ($P < 0.001$ for all comparisons), indicating enhanced wound closure Fig. 9 (C). Consistent with these results, wound thickness measurements at days 7 and 10 showed that SA-PEG-D-PL treatments led to thinner wounds compared to others. Statistically significant differences were observed between SA-PEG-D-PL and SA-PEG-PL ($P = 0.009$), and between SA-PEG-PL and PL ($P = 0.009$), highlighting the limited efficacy of PL alone. The superior performance of SA-PEG-D-PL formulations may be attributed to improved bioavailability and sustained delivery of bioactive molecules.

Collectively, these direct comparisons demonstrate that SA-PEG-D-PL functionalized fibers exhibit superior therapeutic efficacy compared to unmodified fibers and controls. The modified fibers significantly enhance wound healing through multiple mechanisms: faster inflammation resolution, accelerated re-epithelialization, improved ECM remodeling with dense collagen organization, reduced scarring, restored basement membrane integrity, and enhanced angiogenesis with follicular regeneration. These outcomes confirm that the synergistic effects of dopamine functionalization and PL immobilization translate into meaningful biological and therapeutic benefits for diabetic wound healing.

5. Conclusion

This study successfully developed wetspun composite fibers based on SA and PEG with immobilized PL for diabetic wound healing applications. The surface modification using PDA significantly improved PL immobilization without compromising fiber integrity. Mechanical evaluation showed that the SA-PEG-D-PL achieved a tensile strength of 20.9 MPa and a young's modulus of 1228.5 MPa, indicating suitability for applications. The surface modified sample also demonstrated the highest water absorbency compared to unmodified controls and maintained a WVTR of ~2300 g per m^2 per day, supporting a moist wound environment. Hemocompatibility tests confirmed the safety of both catechol-modified and unmodified samples, with hemolysis ratios of 0.81% and 2.22%, respectively. The SA-PEG-D-PL group also demonstrated the BCI of 15% compared to 23% in the SA-PEG-PL group, indicating improved hemostatic modulation. *In vitro* cumulative release shows that PL alone has a rapid release, reaching ~50% within 50 hours and ~60% by 432 hours. The SA-PEG-PL sample exhibited a slower, sustained release, increasing from ~30% at 50 hours to ~70% at 432 hours. On the other hand, the SA-PEG-D-PL sample demonstrated the highest and most consistent release, reaching ~35% at 50 hours and ~90% by 432 hours, indicating the effect of catechol functionalization on enhancing lysate diffusion. *In vivo* studies using STZ induced diabetic mice confirmed the fabric's therapeutic potential, with the SA-PEG-D-PL sample exhibiting 90% wound closure by day 10, compared to <60% in control groups. Histological analysis revealed enhanced neovascularization, organized granulation tissue, reduced scarring, and improved re-epithelialization in the modified sample, indicating functional skin regeneration. These findings validate the potential of the SA-PEG-D-PL wetspun fiber as a bioactive wound dressing platform that combines mechanical robustness, high absorbency, sustained growth factor release, and accelerated diabetic wound healing.

Conflicts of interest

There are no conflicts to declare.

Data availability

Additional data will be available up on request.

Supplementary information (SI): detailed data on platelet lysate preparation methodology, surface modification characterization of fibers (digital image analysis and EDS spectra), mechanical testing results (stress–strain behavior), swelling and degradation studies at different pH conditions, standard curve for *in vitro* platelet lysate release, and quantitative analysis of vessel density from *in vivo* wound healing studies. See DOI: https://doi.org/10.1039/d6ra00827e.

Acknowledgements

The project was supported by the Committee for Advanced Studies & Research (CASR), and the opportunity to serve as a teaching Assistant (TA) in the Department of Biomedical Engineering at Bangladesh University of Engineering and Technology (BUET).

References

1 C. Deng, D. Dong, T. Wang, *et al.*, Promotion of diabetic wound healing using novel Cu2O/Pt nanocubes through bacterial killing and enhanced angiogenesis in rats, *Biomater. Adv.*, 2022, **134**, 112552.

2 S. Patel, S. Srivastava, M. R. Singh, *et al.*, Mechanistic insight into diabetic wounds: Pathogenesis, molecular targets and treatment strategies to pace wound healing, *Biomed. Pharmacother.*, 2019, **112**, 108615.

3 S. L. Wong, M. Demers, K. Martinod, *et al.*, Diabetes primes neutrophils to undergo NETosis, which impairs wound healing, *Nat. Med.*, 2015, **21**(217), 815–819.

4 X. Wei, C. Liu, Z. Li, *et al.*, Chitosan-based hydrogel dressings for diabetic wound healing via promoting M2 macrophage-polarization, *Carbohydr. Polym.*, 2024, **331**, 121873.

5 T. A. Wynn and K. M. Vannella, Macrophages in Tissue Repair, Regeneration, and Fibrosis, *Immunity*, 2016, **44**, 450–462.

6 X. Song, D. Li, T. Guo, *et al.*, Hyaluronan-based hydrogel achieves in situ administration of protocatechualdehyde to polarize macrophages to M2 phenotype for diabetic wound therapy, *Int. J. Biol. Macromol.*, 2025, **318**, 145118.

7 L. I. Salsabil, A. Rahman, A. Hoque, *et al.*, Platelet Lysate-Incorporated Sodium Alginate Polymannuronate Nanogel with Mussel-Inspired Chemistry for Scar-Minimized Diabetic Wound Healing, *Mol. Pharm.*, 2025, **22**(11), 6887–6906.

8 H. L. Weiner and D. Zagzag, Growth factor receptor tyrosine kinases: Cell adhesion kinase family suggests a novel signaling mechanism in cancer, *Cancer Invest.*, 2000, **18**, 544–554.

9 T. Burnouf, C. Y. Lee, C. W. Luo, *et al.*, Human blood-derived fibrin releasates: Composition and use for the culture of cell lines and human primary cells, *Biologicals*, 2012, **40**, 21–30.

10 E. Bari, S. Perteghella, S. Faragò, *et al.*, Association of silk sericin and platelet lysate: Premises for the formulation of wound healing active medications, *Int. J. Biol. Macromol.*, 2018, **119**, 37–47.

11 Q. Chang, J. Cai, Y. Wang, *et al.*, Large adipose tissue generation in a mussel-inspired bioreactor of elastic–mimetic cryogel and platelets, *J. Tissue Eng.*, 2018, **9**, 2041731418808633.

12 X. Liu, Y. Yang, X. Niu, *et al.*, An in situ photocrosslinkable platelet rich plasma – Complexed hydrogel glue with growth factor controlled release ability to promote cartilage defect repair, *Acta Biomater.*, 2017, **62**, 179–187.

13 Y. Liu, S. Zeng, W. Ji, *et al.*, Emerging Theranostic Nanomaterials in Diabetes and Its Complications, *Adv. Sci.*, 2022, **9**, 2102466.

14 L. Malgarim Cordenonsi, A. Faccendini, S. Rossi, *et al.*, Platelet lysate loaded electrospun scaffolds: Effect of nanofiber types on wound healing, *Eur. J. Pharm. Biopharm.*, 2019, **142**, 247–257.

15 B. Kutlu, R. S. Tiğli Aydin, A. C. Akman, *et al.*, Platelet-rich plasma-loaded chitosan scaffolds: Preparation and growth factor release kinetics, *J. Biomed. Mater. Res., Part B*, 2013, **101B**, 28–35.

16 M. Prasathkumar and S. Sadhasivam, Chitosan/Hyaluronic acid/Alginate and an assorted polymers loaded with honey, plant, and marine compounds for progressive wound healing—Know-how, *Int. J. Biol. Macromol.*, 2021, **186**, 656–685.

17 S. Hasan, M. A. Hasan, M. U. Hassan, *et al.*, Biopolymers in diabetic wound care management: A potential substitute to traditional dressings, *Eur. Polym. J.*, 2023, **189**, 111979.

18 V. Alinezhad, K. Esmaeilzadeh, H. Bagheri, *et al.*, Engineering a platelet-rich plasma-based multifunctional injectable hydrogel with photothermal, antibacterial, and antioxidant properties for skin regeneration, *Biomater. Sci.*, 2023, **11**, 5872–5892.

19 Y. Zhao, L. Huang, G. Lin, *et al.*, Skin-adaptive film dressing with smart-release of growth factors accelerated diabetic wound healing, *Int. J. Biol. Macromol.*, 2022, **222**, 2729–2743.

20 M. T. Arafat, G. Tronci, J. Yin, *et al.*, Biomimetic wet-stable fibres via wet spinning and diacid-based crosslinking of collagen triple helices, *Polymer*, 2015, **77**, 102–112.

21 M. T. Arafat, G. Tronci, J. Yin, *et al.*, Biomimetic wet-stable fibres via wet spinning and diacid-based crosslinking of collagen triple helices, *Polymer*, 2015, **77**, 102–112.

22 Y. Zheng, J. Miao, N. Maeda, *et al.*, Uniform nanoparticle coating of cellulose fibers during wet electrospinning, *J. Mater. Chem. A*, 2014, **2**, 15029–15034.

23 G. Q. Peng, X. H. Zhang, Y. F. Wen, *et al.*, Effect of Coagulation Bath DMSO Concentration on the Structure and Properties of Polyacrylonitrile (PAN) Nascent Fibers during Wet-Spinning, *J. Macromol. Sci., Part B*, 2008, **47**, 1130–1141.

24 C. H. Goh, P. W. S. Heng and L. W. Chan, Alginates as a useful natural polymer for microencapsulation and therapeutic applications, *Carbohydr. Polym.*, 2012, **88**, 1–12.

25 E. Ilhan, S. Cesur, E. Guler, *et al.*, Development of Satureja cuneifolia-loaded sodium alginate/polyethylene glycol scaffolds produced by 3D-printing technology as a diabetic wound dressing material, *Int. J. Biol. Macromol.*, 2020, **161**, 1040–1054.

26 R. B. Greenwald, Y. H. Choe, J. McGuire, *et al.*, Effective drug delivery by PEGylated drug conjugates, *Adv. Drug Deliv. Rev.*, 2003, **55**, 217–250.

27 T. Jiang, S. Liu, Z. Wu, *et al.*, ADSC-exo@MMP-PEG smart hydrogel promotes diabetic wound healing by optimizing cellular functions and relieving oxidative stress, *Mater. Today Bio*, 2022, **16**, 100365.

28 Y. Wang, Y. Zhang, Y. P. Yang, *et al.*, Versatile dopamine-functionalized hyaluronic acid-recombinant human collagen hydrogel promoting diabetic wound healing via inflammation control and vascularization tissue regeneration, *Bioact. Mater.*, 2024, **35**, 330–345.

29 H. Lee, S. M. Dellatore, W. M. Miller, *et al.*, Mussel-inspired surface chemistry for multifunctional coatings, *Science*, 2007, **318**, 426–430.

30 F. Hakimi, L. Maeso, A. Dehghan, *et al.*, Schiff Base Polysaccharide Hydrogels: A Promising Biomaterial for Wound Dressings, *ChemistrySelect*, 2025, **10**, e05175.

31 Y. Zhang, L. Chen, C. Zhang, *et al.*, Polydopamine-assisted partial hydrolyzed poly(2-methyl-2-oxazolinze) as coating for determination of melamine in milk by capillary electrophoresis, *Talanta*, 2016, **150**, 375–387.

32 M. Liu, J. Ji, X. Zhang, *et al.*, Self-polymerization of dopamine and polyethyleneimine: novel fluorescent organic nanoprobes for biological imaging applications, *J. Mater. Chem. B*, 2015, **3**, 3476–3482.

33 H. J. Kim and J. H. Song, Improvement in the mechanical properties of carbon and aramid composites by fiber surface modification using polydopamine, *Compos. B Eng.*, 2019, **160**, 31–36.

34 A. H. Zisch, U. Schenk, J. C. Schense, *et al.*, Covalently conjugated VEGF–fibrin matrices for endothelialization, *J. Contr. Release*, 2001, **72**, 101–113.

35 G. A. Hudalla and W. L. Murphy, Biomaterials that Regulate Growth Factor Activity via Bioinspired Interactions, *Adv. Funct. Mater.*, 2011, **21**, 1754–1768.

36 C. Pignatelli, G. Perotto, M. Nardini, *et al.*, Electrospun silk fibroin fibers for storage and controlled release of human platelet lysate, *Acta Biomater.*, 2018, **73**, 365–376.

37 S. Nazarnezhad, F. Kermani, V. R. Askari, *et al.*, Preparation and Characterization of Platelet Lysate (Pl)-Loaded Electrospun Nanofibers for Epidermal Wound Healing, *J. Pharm. Sci.*, 2022, **111**, 2531–2539.

38 H. J. Haugen, D. Coelho, N. D. Tien, *et al.*, Enhanced chitosan fibres for skin regeneration: solution blow spinning and incorporation with platelet lysate and tannic acid, *Mater. Res. Express*, 2024, **11**, 125401.

39 S. A. Sell, P. S. Wolfe, J. J. Ericksen, *et al.*, Incorporating platelet-rich plasma into electrospun scaffolds for tissue engineering applications, *Tissue Eng. Part A*, 2011, **17**, 2723–2737.

40 K. Schallmoser and D. Strunk, Preparation of Pooled Human Platelet Lysate (pHPL) as an Efficient Supplement for Animal Serum-Free Human Stem Cell Cultures, *J. Vis. Exp.*, 2009, **32**(32), 1523.

41 A. Bianchetti, C. Chinello, M. Guindani, *et al.*, A Blood Bank Standardized Production of Human Platelet Lysate for Mesenchymal Stromal Cell Expansion: Proteomic Characterization and Biological Effects, *Front. Cell Dev. Biol.*, 2021, **9**, 650490.

42 T. H. Aneem, S. Y. Wong, H. Afrin, *et al.*, Investigation of coagulation process of wet-spun sodium alginate polymannuronate fibers with varied functionality using organic coagulants and cross-linkers, *Mater. Today Chem.*, 2021, **22**, 100580.

43 D. Gupta, A. K. Singh, N. Kar, *et al.*, Modelling and optimization of NaOH-etched 3-D printed PCL for enhanced cellular attachment and growth with minimal loss of mechanical strength, *Mater. Sci. Eng., C*, 2019, **98**, 602–611.

44 X. Gao, X. Zhang, J. Song, *et al.*, Osteoinductive peptide-functionalized nanofibers with highly ordered structure as biomimetic scaffolds for bone tissue engineering, *Int. J. Nanomed.*, 2015, **10**, 7109–7128.

45 A. Wang, C. Xu, C. Zhang, *et al.*, Experimental Investigation of the Properties of Electrospun Nanofibers for Potential Medical Application, *J. Nanomater.*, 2015, **2015**, 418932.

46 L. H. Tithy, A. Rahman, S. Y. Wong, *et al.*, Chitosan/starch based unoxidized tannic acid modified microparticles for rapid hemostasis with broad spectrum antibacterial activity, *Carbohydr. Polym.*, 2024, **336**, 122111.

47 T. Hasan Aneem, M. Sarker, S. Y. Wong, *et al.*, Antimicrobial peptide immobilization on catechol-functionalized PCL/alginate wet-spun fibers to combat surgical site infection, *J. Mater. Chem. B*, 2024, **12**, 7401–7419.

48 A. B. Humayun, L. H. Tithy, S. Y. Wong, *et al.*, Thermally induced phase separation (TIPS) to fabricate chitosan/pectin based absorbent macroporous sponge with tranexamic acid for stable hemostasis, *Int. J. Biol. Macromol.*, 2025, **308**, 142563.

49 R. H. Jinia, N. Datta, S. Y. Wong, *et al.*, Mechanistic study of unoxidized tannic acid crosslinked gelatin-CMC electrospun matrices for combating antibacterial resistance in infected wounds, *Int. J. Biol. Macromol.*, 2025, **330**, 147837.

50 J. H. Petropoulos, K. G. Papadokostaki and M. Sanopoulou, Higuchi's equation and beyond: Overview of the formulation and application of a generalized model of drug release from polymeric matrices, *Int. J. Pharm.*, 2012, **437**, 178–191.

51 M. N. Freitas and J. M. Marchetti, Nimesulide PLA microspheres as a potential sustained release system for the treatment of inflammatory diseases, *Int. J. Pharm.*, 2005, **295**, 201–211.

52 M. Askarizadeh, N. Esfandiari, B. Honarvar, *et al.*, Kinetic Modeling to Explain the Release of Medicine from Drug Delivery Systems, *ChemBioEng Rev.*, 2023, **10**, 1006–1049.

53 B. L. Furman, Streptozotocin-Induced Diabetic Models in Mice and Rats, *Curr. Protoc. Pharmacol.*, 2015, **70**, 1–20.

54 X. Wang, Y. Jiao, Y. Pan, L. Zhang, H. Gong, Y. Qi, M. Wang, H. Gong, M. Shao, X. Wang, D. Jiang, *et al.*, Fetal dermal mesenchymal stem cell-derived exosomes accelerate cutaneous wound healing by activating notch signaling, *Stem Cell. Int.*, 2019, **2019**, 1–11.

55 Z. Sang, W. Zhang, Z. Zhou, *et al.*, Functionalized alginate with liquid-like behaviors and its application in wet-spinning, *Carbohydr. Polym.*, 2017, **174**, 933–940.

56 Y. He, E. Du, X. Zhou, *et al.*, Wet-spinning of fluorescent fibers based on gold nanoclusters-loaded alginate for sensing of heavy metal ions and anti-counterfeiting, *Spectrochim. Acta, Part A*, 2020, **230**, 118031.

57 S. Nam, R. Stowers, J. Lou, *et al.*, Varying PEG density to control stress relaxation in alginate-PEG hydrogels for 3D cell culture studies, *Biomaterials*, 2019, **200**, 15–24.

58 Z. H. Ghauri, A. Islam, M. A. Qadir, *et al.*, Novel pH-responsive chitosan/sodium alginate/PEG based hydrogels for release of sodium ceftriaxone, *Mater. Chem. Phys.*, 2022, **277**, 125456.

59 K. Cheng, M. Li, S. Zhang, *et al.*, Study on the structure and properties of functionalized fibers with dopamine, *Colloids Surf., A*, 2019, **582**, 123846.

60 P. Ma, M. Xin, Y. Zhang, *et al.*, Facile synthesis of novel dopamine-modified glass fibers for improving alkali resistance of fibers and flexural strength of fiber-reinforced cement, *RSC Adv.*, 2021, **11**, 18818–18826.

61 M. E. Lynge, P. Schattling and B. Städler, Recent developments in poly(dopamine)-based coatings for biomedical applications, *Nanomedicine*, 2015, **10**, 2725–2742.

62 X. Zhang, C. Huang and X. Jin, Influence of K+ and Na+ ions on the degradation of wet-spun alginate fibers for tissue engineering, *J. Appl. Polym. Sci.*, 2017, **134**, 44396.

63 X. Wang, H. Zhang, X. Zhang, *et al.*, A comparison study on effects of polyglycerols on physical properties of alginate films, *Int. J. Biol. Macromol.*, 2024, **254**, 127879.

64 K. Bilge, F. Javanshour, A. B. Raheman, *et al.*, A comparative fractographic analysis for the effect of polymeric nanofiber reinforcements on the tensile behavior of multi-layered epoxy nanocomposites, *Polym. Eng. Sci.*, 2025, **65**, 2343–2352.

65 D. J. Vanderah, H. La, J. Naff, *et al.*, Control of Protein Adsorption: Molecular Level Structural and Spatial Variables, *J. Am. Chem. Soc.*, 2004, **126**, 13639–13641.

66 R. Y. M. Huang, R. Pal and G. Y. Moon, Characteristics of sodium alginate membranes for the pervaporation dehydration of ethanol–water and isopropanol–water mixtures, *J. Membr. Sci.*, 1999, **160**, 101–113.

67 Q. Wang, N. Zhang, X. Hu, *et al.*, Alginate/polyethylene glycol blend fibers and their properties for drug controlled release, *J. Biomed. Mater. Res., Part A*, 2007, **82A**, 122–128.

68 E. Bari, S. Perteghella, G. Marrubini, *et al.*, In vitro efficacy of silk sericin microparticles and platelet lysate for intervertebral disk regeneration, *Int. J. Biol. Macromol.*, 2018, **118**, 792–799.

69 Đ. Tintor, K. Ninković, J. Milošević, *et al.*, Gaining insight into protein structure via ATR-FTIR spectroscopy, *Vib. Spectrosc.*, 2024, **134**, 103726.

70 Y. Wang, H. Chen, L. Cui, *et al.*, Toughen and strengthen alginate fiber by incorporation of polyethylene glycol grafted cellulose nanocrystals, *Cellulose*, 2022, **29**, 5021–5035.

71 R. Du, L. He, P. Li, *et al.*, Polydopamine-modified Al2O3/Polyurethane composites with largely improved thermal and mechanical properties, *Materials*, 2020, **13**(7), 1772.

72 S. R. Baker, S. Banerjee, K. Bonin, *et al.*, Determining the mechanical properties of electrospun poly-ε-caprolactone (PCL) nanofibers using AFM and a novel fiber anchoring technique, *Mater. Sci. Eng., C*, 2016, **59**, 203–212.

73 N. Alharbi, A. Daraei, H. Lee, *et al.*, The effect of molecular weight and fiber diameter on the mechanical properties of single, electrospun PCL nanofibers, *Mater. Today Commun.*, 2023, **35**, 105773.

74 G. Sandri, M. C. Bonferoni, S. Rossi, *et al.*, Thermosensitive eyedrops containing platelet lysate for the treatment of corneal ulcers, *Int. J. Pharm.*, 2012, **426**, 1–6.

75 L. Zampori, G. Dotelli, P. Gallo Stampino, *et al.*, Thermal characterization of a montmorillonite, modified with polyethylene-glycols (PEG1500 and PEG4000), by in situ HT-XRD and FT IR: Formation of a high-temperature phase, *Appl. Clay Sci.*, 2012, **59**(60), 140–147.

76 T. Jayaramudu, G. M. Raghavendra, K. Varaprasad, *et al.*, Preparation and characterization of poly(ethylene glycol) stabilized nano silver particles by a mechanochemical assisted ball mill process, *J. Appl. Polym. Sci.*, 2016, **133**, 43027.

77 R. Bhattacharyya and S. K. Ray, Removal of congo red and methyl violet from water using nano clay filled composite hydrogels of poly acrylic acid and polyethylene glycol, *Chem. Eng. J.*, 2015, **260**, 269–283.

78 R. Xu, H. Xia, W. He, *et al.*, Controlled water vapor transmission rate promotes wound-healing via wound re-epithelialization and contraction enhancement, *Sci. Rep.*, 2016, **61**(6), 1–12.

79 D. Queen, J. D. S. Gaylor, J. H. Evans, *et al.*, The preclinical evaluation of the water vapour transmission rate through burn wound dressings, *Biomaterials*, 1987, **8**, 367–371.

80 L. M. Furtado, R. A. Ando and D. F. S. Petri, Polydopamine-coated cellulose acetate butyrate microbeads for caffeine removal, *J. Mater. Sci.*, 2019, **55**(558), 3243–3258.

81 Z. Xu, L. Su, S. Jiang, *et al.*, Crystallization behavior and water vapor permeability of poly(lactic acid) nanocomposite under oscillatory shear, *J. Appl. Polym. Sci.*, 2015, **132**(30), app.42321.

82 Z. Xu, L. Shi, M. Yang, *et al.*, Fabrication of a novel blended membrane with chitosan and silk microfibers for wound healing: characterization, in vitro and in vivo studies, *J. Mater. Chem. B*, 2015, **3**, 3634–3642.

83 C. Liu, W. Yao, M. Tian, *et al.*, Mussel-inspired degradable antibacterial polydopamine/silica nanoparticle for rapid hemostasis, *Biomaterials*, 2018, **179**, 83–95.

84 H. Tan, B. Wu, C. Li, *et al.*, Collagen cryogel cross-linked by naturally derived dialdehyde carboxymethyl cellulose, *Carbohydr. Polym.*, 2015, **129**, 17–24.

85 X. H. Wang, D. P. Li, W. J. Wang, *et al.*, Crosslinked collagen/chitosan matrix for artificial livers, *Biomaterials*, 2003, **24**, 3213–3220.

86 H. Lee, S. M. Dellatore, W. M. Miller, *et al.*, Mussel-inspired surface chemistry for multifunctional coatings, *Science*, 2007, **318**, 426–430.

87 Z. K. Kuo, M. Y. Fang, T. Y. Wu, *et al.*, Hydrophilic films: How hydrophilicity affects blood compatibility and cellular compatibility, *Adv. Polym. Technol.*, 2018, **37**, 1635–1642.

88 M. Zare-Gachi, H. Daemi, J. Mohammadi, *et al.*, Improving anti-hemolytic, antibacterial and wound healing properties of alginate fibrous wound dressings by exchanging counter-cation for infected full-thickness skin wounds, *Mater. Sci. Eng., C*, 2020, **107**, 110321.

89 J. W. Weisel and R. I. Litvinov, Red blood cells: the forgotten player in hemostasis and thrombosis, *J. Thromb. Haemostasis*, 2019, **17**, 271–282.

90 Y. Wang, Y. Fu, J. Li, *et al.*, Multifunctional chitosan/dopamine/diatom-biosilica composite beads for rapid blood coagulation, *Carbohydr. Polym.*, 2018, **200**, 6–14.

91 Y. Liu, Y. Sui, C. Liu, *et al.*, A physically crosslinked polydopamine/nanocellulose hydrogel as potential versatile vehicles for drug delivery and wound healing, *Carbohydr. Polym.*, 2018, **188**, 27–36.

92 S. Ganguly, D. Wulff, C. M. Phan, *et al.*, Injectable and 3D Extrusion Printable Hydrophilic Silicone-Based Hydrogels for Controlled Ocular Delivery of Ophthalmic Drugs, *ACS Appl. Bio Mater.*, 2024, **7**, 6286–6296.

93 M. C. Van Der Leeden, Are conformational changes, induced by osmotic pressure variations, the underlying mechanism of controlling the adhesive activity of mussel adhesive proteins?, *Langmuir*, 2005, **21**, 11373–11379.

94 J. Wang, Y. Chen, G. Zhou, *et al.*, Polydopamine-Coated Antheraea pernyi (A. pernyi) Silk Fibroin Films Promote Cell Adhesion and Wound Healing in Skin Tissue Repair, *ACS Appl. Mater. Interfaces*, 2019, **11**, 34736–34743.